Late-Winter Generation of Spiciness on Subducted Isopycnals

STEPHEN G. YEAGER AND WILLIAM G. LARGE

National Center for Atmospheric Research, Boulder, Colorado*

(Manuscript received 3 February 2003, in final form 27 January 2004)

ABSTRACT

The origins of density-compensating anomalies of temperature and salinity (spice) are investigated using a model forced with the most realistic surface products available over the 40 years 1958–97. In this hindcast, the largest interannual spiciness anomalies are found in the Pacific Ocean near the isopycnal $\sigma_0 = 25.5$, where deviations as great as 1.2°C and 0.6 psu are generated equatorward of winter outcropping in the eastern subtropics in both hemispheres. These source regions are characterized by very unstable salinity gradients and low mean density stratification in winter. Two related signatures of winter mixing in the southeast Pacific (SEP) are density that is well mixed deeper than either temperature or salinity and subsurface density ratios that approach 1. All ocean basins in the model are shown to have regions with these characteristics and signatures; however, the resultant spiciness signals are focused on different isopycnals ranging from $\sigma_0 = 25.0$ in the northeast Pacific to $\sigma_0 = 26.5$ in the south Indian Ocean. A detailed examination of the SEP finds that large positive anomalies are generated by diapycnal mixing across subducted isopycnals (e.g., $\sigma_0 = 25.5$), whereas negative anomalies are the result of a steady isopycnal advection, moderated by vertical advection and heave. There is considerable interannual variability in the strength of anomalies and in the density on which they occur. Historical observations are consistent with the model results but are insufficient to verify all aspects of the hindcast, including the processes of anomaly generation in the SEP. It was not possible to relate isopycnal anomaly genesis to local surface forcing of any kind. A complex scenario involving basinwide circulation of both the ocean and atmosphere, especially of surface water through the subtropical evaporation zones, is put forward to explain the decadal time scale evident in SEP salinity anomalies on $\sigma_0 = 25.5$. Pacific anomalies generated on $\sigma_0 = 25.5$ can be traced along mean geostrophic streamlines to the western boundary, where decadal salinity variations at $\approx$7°S are about 2 times as large (order $\pm$0.1 psu) as at $\approx$12°N, although there may be more variance on shallower isopycnals in the north. At least portions of the $\sigma_0 = 25.5$ signals appear to continue along the boundary to a convergence at the equator, suggesting that the most robust sources of Pacific spiciness variance coincide with equatorial exchange pathways.

1. Introduction

Observed interannual to decadal changes in ocean water properties on density surfaces have commonly been ascribed to the effects of changing air–sea fluxes on surface salinity and temperature in water mass formation regions (Bindoff and Church 1992; Bryden et al. 1996, 2003; Johnson and Orsi 1997; Wong et al. 1999; Arbic and Owens 2001). The assumption that variations on subducted density surfaces are set at the density outcrops allows deep isopycnal variability to be decomposed into separate surface heating, surface freshening, and heave components (Bindoff and McDougall 1994, 2000). However, discrepancies between observed spiciness variations and trends in ventilation region surface fluxes have been noted (Suga et al. 2000; Kessler 1999), suggesting that other important processes may be at work besides atmosphere–ocean exchange and subduction. Therefore, interpretation of observed water mass variability in terms of oceanic processes operating on all time scales, including the climatic, requires a thorough understanding of all the subsurface ocean processes that produce anomalies on density surfaces. Anomalous advection across coincident temperature/salinity fronts may explain the origins of isopycnic variability in some regions (Rintoul and England 2002; Schneider 2000). In this paper, we utilize an ocean general circulation model (OGCM) to explore isopycnal anomaly genesis through late-winter diapycnal mixing in the presence of large, density-compensating vertical temperature and salinity gradients.

The vertical mixing mechanism that we examine is particularly active in the eastern subtropical Pacific Ocean in both hemispheres, and so thermocline transmission of signals is robust. The existence of geostrophic pathways that link the subtropics with the equatorial

*The National Center for Atmospheric Research is sponsored by the National Science Foundation.

Corresponding author address: S. Yeager, Climate and Global Dynamics Division, National Center for Atmospheric Research, Boulder, CO 80307-3000.
E-mail: yeager@ucar.edu

ocean is well documented in the Pacific (Fine et al. 1987; Liu et al. 1994; Blanke and Raynaud 1997; Rothstein et al. 1998; Johnson and McPhaden 1999; Harper 2000; Nonaka and Takeuchi 2001), and a relative weakness of the northern connection has been explained as an effect of the ITCZ on ocean potential vorticity dynamics (Lu and McCreary 1995; Rothstein et al. 1998; Johnson and McPhaden 1999). Anomalies that form in the western boundary exchange window (Liu et al. 1994; Harper 2000; Rothstein et al. 1998) follow a route to the equator via the western boundary in both Pacific hemispheres. Interest in the dynamics of such anomaly transmission has been stimulated in part by the hypothesis that decadal variability on the equator may be related to subsurface anomaly advection (Gu and Philander 1997; Zhang et al. 1998). Alternative mechanisms of decadal equatorial variability that do not involve the temperature and salinity anomalies of interest here include variations in surface transport (Kleeman et al. 1999) and atmospheric teleconnections (Barnett et al. 1999).

Observations have yielded evidence of decadal temperature anomalies, apparently surface-forced, subducting in the central North Pacific and propagating southward in the thermocline (Deser et al. 1996; Zhang et al. 1998). Schneider et al. (1999) showed that these anomalies propagate along lines of mean potential vorticity no farther south than 18°N and therefore could find no evidence of a connection between the midlatitude North Pacific and the equator in terms of coherent isotherm depth anomaly propagation. These studies lacked the salinity data needed to perform the analysis along isopycnals.

Linking subsurface decadal changes in salinity to surface forcing has proven to be even more problematic. In their attempt to trace the causes of decadal change in North Pacific Tropical Water (NPTW) salinity observed at 137°E, Suga et al. (2000) could not reconcile the positive isopycnal salinity change with the freshening that occurred in the formation region, even with the effects of concurrent surface temperature change taken into account. The South Pacific suffers from much sparser data coverage and consequently has received less attention, despite indications that property fluxes to the equator are significantly greater than in the north (Johnson and McPhaden 1999). Kessler (1999) used repeat CTD sections to track interannual changes on $\sigma_0 = 24.5$ at 165°E just south of the equator and found that much of the salinity change at this density could be attributed to zonal advection along the isosurface, implying that the source of the variability was the outcrop of $\sigma_0 = 24.5$. However, the surface forcing anomalies in the southeastern Pacific region of this outcrop were of the opposite sign needed to explain the downstream isopycnal variations. Despite some success in linking observed subsurface ocean change to atmospheric regime shifts, isopycnal salinity variability in the Pacific has not been well-explained using this approach.

Several modeling studies have helped to illuminate the mechanisms by which isopycnal anomalies link surface processes with the ocean interior. Lysne et al. (1999) showed that when observed upper-ocean conditions are assimilated in the North Pacific of an OGCM, thermal anomalies closely resembling those examined by Deser et al. (1996) advect along isopycnals all the way to the equator, although they postulate that such a mechanism may in fact be less important than wave transmission. Using a fully coupled ocean–atmosphere model, Pierce et al. (2000) showed clear evidence of isopycnal anomalies propagating from the eastern Pacific subtropics to the equator on time scales of 7–10 yr, but, based on the low standard deviation of anomalies reaching the equator and the weakness of lagged correlations between formation region SSTs and equatorial SSTs, concluded that such advected thermal anomalies had minimal effect on the equatorial density structure. This result is in contrast with an analysis of a fully coupled model by Schneider (2000) in which the equatorial effects of advected spiciness anomalies in the Pacific close a feedback loop whereby equatorially influenced trade winds force subsurface spiciness anomalies off-equator. In the Atlantic, Lazar et al. (2001) were able to track the subduction of an artificially forced SST anomaly westward from the eastern subtropics to the equator.

The purpose of the present study is to elucidate a mixing mechanism that may account for some observed deep isopycnal variations (Kessler 1999; Suga et al. 2000; Bryden et al. 2003; Wong et al. 1999). It employs an OGCM forced with atmospheric fields spanning 1958–97 (section 2) whose solution is a fully prognostic realization of the historical evolution of the ocean over the 40-yr forcing period. The main focus of the present work is the generation of spiciness anomalies in the southeast Pacific (section 3). The propagation of these anomalies and their relevance to remotely forced Pacific equatorial variability is briefly addressed in section 4; more global implications are discussed in section 5. The model fidelity in the southeast Pacific is examined in appendix A, and some model sensitivities are shown in appendix B.

2. The hindcast

Forty years of ocean variability (1958–97) are hindcast by a global OGCM developed as the ocean component of the first National Center for Atmospheric Research (NCAR) Climate System Model (CSM1) from the Geophysical Fluid Dynamics Laboratory (GFDL) Modular Ocean Model (MOM1) primitive equation ocean (Gent et al. 1998). The model is relatively well resolved in the vertical direction; 45 z-coordinate vertical levels with 8-m spacing at the surface, stretching to 260 m in the deepest ocean. The K-profile parameterization (KPP; Large et al. 1994) is used to determine large vertical mixing coefficients above a diagnosed boundary layer depth, h. The most important aspect of

this scheme to the mechanism of section 3 is that properties will not completely mix as deep as h if changes in stratification, shear, and forcing cause h to shallow before sufficient time (set by the diffusive time scale) has elapsed. This possibility is enhanced by the coefficients becoming smaller as h is approached. In general, the vertical mixing below h is regarded as the superposition of three processes: internal wave breaking, shear instability, and double diffusion, which is matched to the boundary layer mixing at h. However, double diffusion is usually not enabled, because of uncertainty in the magnitude and functional dependencies of its transfer coefficient. The sensitivity of the vertical mixing to higher vertical resolution and to double diffusion is examined in appendix B.

Long integrations to reduce trends and dependencies on initial conditions are more important to the present application than explicitly resolving ocean mesoscale eddies, and so the horizontal resolution is relatively coarse; 2.4° zonal and variable meridional grid spacing; from 0.6° at the equator increasing to 1.2° poleward of 30°. Instead, the associated eddy mixing is parameterized following Gent and McWilliams (1990). One component of this mixing is an isopycnal-oriented diffusion (Redi 1982) with a coefficient, $K_R = 800\ \mathrm{m^2\ s^{-1}}$. The other component is an eddy-induced velocity with an associated advection and meridional overturning circulation. McWilliams and Danabasoglu (2002) analyze this circulation between 25°S and 25°N and find that it compares favorably (''close correspondence in shape and not an essential disagreement in magnitude'') with the Roemmich and Gilson (2001) analysis of North Pacific observations. However, the parameterization is most applicable where isopycnal slopes are shallow. In steep slope regions, including the mixed layer, it is not yet clear how to parameterize eddy effects, so both components of the mixing are simply reduced steadily to 0 according to tapering schemes in Large et al. (1997).

The model has no explicit horizontal diffusion, but an anisotropic horizontal viscosity that allows realistic equatorial currents to develop (Large et al. 2001). Doney et al. (2003) document modifications to this viscosity that have made the subtropical and subpolar gyres much less viscous, and hence more physical. In particular, they show a marked improvement in the North Atlantic Gyre structure with separation of the Gulf Stream off Cape Hatteras and southward penetration of the subpolar gyre along the east coast of North America.

The model forcing follows Large et al. (1997) and is detailed in Doney et al. (2003). The primary dataset is the 40-yr cycle (1958–97) of 6-hourly winds, and near surface temperature and humidity from the National Centers for Environmental Prediction (NCEP)–NCAR reanalysis (Kalnay et al. 1996). Radiative forcing is derived from monthly satellite estimates of cloud fraction (Rossow and Schiffer 1991) and insolation (Bishop and Rossow 1991; Bishop et al. 1997), available from July 1983 through June 1991. A monthly climatology of cloud and insolation is used to fill the other months of the 40-yr cycle. The precipitation forcing is a combination of the Spencer (1993) satellite product (1983–91) and the Xie and Arkin (1996) blended precipitation (1979–97). The former is used only in the tropical Indian and western Pacific (1983–91) and in the Gulf of Alaska. Again, missing months of the 40-yr cycle are filled with a mean annual cycle from each dataset.

The model is spun up from rest and observed temperature and salinity distributions, but after 333 yr of integration with a factor-of-50 acceleration applied to deep tracers (Danagasoglu et al. 1996), the solution has lost all memory of initial conditions by the beginning of our hindcast integrations. Subsequently, the model is run with no acceleration for a total of 160 yr, or four of the 40-yr forcing cycles. Analysis is restricted to the fourth cycle, which Doney et al. (2003) found to be uncontaminated by model drift in the upper 400 m of interest here. Their sensitivity studies suggest that the transient induced by jumping from 1997 back to 1958 should not persist after about 1965 of the following cycle.

Prior to spinup, surface fluxes were computed using climatological sea surface temperatures. A balanced heat budget was obtained by reducing insolation by 12.5% and NCEP specific humidity by 6%. The spinup includes these corrections and two features designed to overcome the large uncertainties associated with global precipitation datasets. The first is a local, weak restoring (2-yr time scale) to observed sea surface salinity, with 0 global mean. The second multiplies the precipitation by a uniform factor that is updated each year and increases (decreases) if the global average ocean salinity increases (decreases) over the previous year. By the end of the spinup this factor is steady at about 1.11, and so it is possible to keep it constant at this value throughout all four 40-yr forcing cycles. Much of the increase in precipitation is necessary to account for the missing river runoff from continents and, because of the weak restoring, is effectively distributed along the coasts, especially at the mouths of large rivers. The success of this procedure, at least in the mean, is demonstrated in appendix A.

The standard model output is monthly means of potential temperature T, salinity S, and three-dimensional velocity, and so the interannual variability is well sampled and not subject to aliasing. However, a density, ρ or σ_0 (density difference from 1000 kg $\mathrm{m^{-3}}$), computed from this output only approximates the monthly mean. The fourth forcing cycle produced the following output analyzed in the present study: 40 annual means, 40 annual anomalies from climatology, 480 monthly means, and 480 monthly anomalies from the monthly climatology. Portions of the cycle have been rerun with higher-frequency output for process studies.

Transformation to isopycnic coordinates is performed as follows. At a given horizontal grid location, salinity

on the isopycnal, S_ρ, is a weighted sum of salinity at adjacent vertical grid levels

$$S_\rho = wS_k + (1 - w)S_{k+1}. \quad (1)$$

The weight, $w = (z_{k+1} - z_\rho)/\Delta z$, is a linear function of the isopycnal depth, z_ρ, which is computed from a linear interpolation of density at adjacent levels, where the grid spacing is Δz. Since the weighting changes with time,

$$\partial_t S_\rho = w\partial_t S_k + (1 - w)\partial_t S_{k+1} + (S_k - S_{k+1})\partial_t w. \quad (2)$$

A budget of terms producing salinity change on a given isopycnal can then be constructed as

$$\partial_t S_\rho = w\partial_t S_k + (1 - w)\partial_t S_{k+1} + (S_{k+1} - S_k)\partial_t z_\rho/\Delta z. \quad (3)$$

The first two terms on the right-hand side of (3) represent a weighted sum of the advective, diffusive, and other terms that change salinity at a given depth level during a given time step. These terms include changes due to pure vertical motions of density surfaces, which effect salinity on depth levels, but not on isopycnals. We can therefore interpret the third term on the right-hand side, referred to as the ''heave'' term, as a correction arising from the transformation to isopycnic coordinates, which removes changes in salinity associated with pure isopycnal heave. Doney et al. (2003) present a global, fixed-depth analysis, where the temperature and salinity variability in the upper 400 m of the model is partitioned into spice and heave components. They find that over most of the ocean the temperature variance is primarily due to heave, in accord with Lysne and Deser (2002), who also utilized this model hindcast. The exceptions are the Kuroshio and Gulf Stream extensions. At 100-m depth, patches of high salinity variance are mostly spice, but heave is not negligible. At 260 m, spice and heave contribute comparable amounts to the interannual variance, and in some regions (e.g., Northwest Pacific) they are negatively correlated so that there is little total variance.

3. Anomaly generation on $\sigma_0 = 25.5$ in the South Pacific

We focus attention on $\sigma_0 = 25.5$ kg m^{-3} in the Pacific because the production and propagation of temperature and salinity anomalies on this surface is particularly robust in the model, especially in the Southern Hemisphere. The interannual variability of salinity (and hence temperature) on the isopycnal is dominated by twin lobes of high variance on both sides of the equator that extend from local maxima in the subtropics, where rms salinity values exceed 0.14 psu (Fig. 1). The lobes follow isolines of isopycnal depth toward the equator (not shown), and so the pattern of variability on the isopycnal surface is related to the advection of anomalies along mean geostrophic streamlines. The westward and equatorward sense of the weakening of the rms salinity implies an eastward and poleward source of variability with subsequent propagation and dispersion.

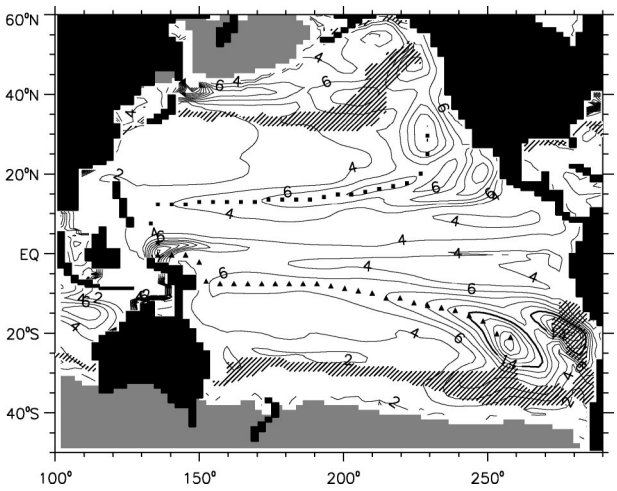

FIG. 1. Rms salinity on $\sigma_0 = 25.5$ computed from 1958–97 annual means. The contour interval is 2, in units of 10^{-2} psu. Northern (square) and southern (triangle) anomaly sampling pathways are overlaid. The cross-hatched region indicates the 40-yr range of mean winter (Mar/Sep) outcrop locations of the isopycnal. The thick contours at 0.14 psu in the eastern South Pacific delimit source regions 1 (western) and 2 (eastern) referred to in the text.

Figure 1 suggests that these source regions coincide with the regions of highest interannual variability and shows that they are generally located well equatorward of the most extreme winter outcrop locations. This result implies that spiciness anomalies are generated subsurface in both hemispheres of the Pacific. These source regions and lobes tend to be farther from the equator in the North Pacific, reflecting the difference in circulation between the two hemispheres. The winter outcrop positions in South Pacific source region 2 (defined as the easternmost thick closed contour in Fig. 1) do tend to be much closer to, or even overlapping with, the origins of isopycnal anomalies. However, we will show that large signals are generated in years when the outcrop falls well poleward of the genesis region highlighted, and that the same subsurface mechanism is at work in both South Pacific source regions.

The largest anomalies on $\sigma_0 = 25.5$ kg m^{-3} originate in the southeast Pacific (SEP) region close to 20°S within twin regions of highest rms salinity (source regions 1 and 2, Fig. 1). Animations of monthly salinity and temperature on the surface give a good sense of how large, highly localized anomalies are generated in some years in this SEP formation region. The largest positive anomalies appear abruptly on the subducted isopycnal in late winter/early spring (September/October); negative anomalies can become large by growing continuously over the course of several years. Both positive and negative anomalies of large magnitude originate below the surface, and especially in source region 1, at locations far from the winter outcrop. Extreme anomalies persist in some cases and propagate equatorward

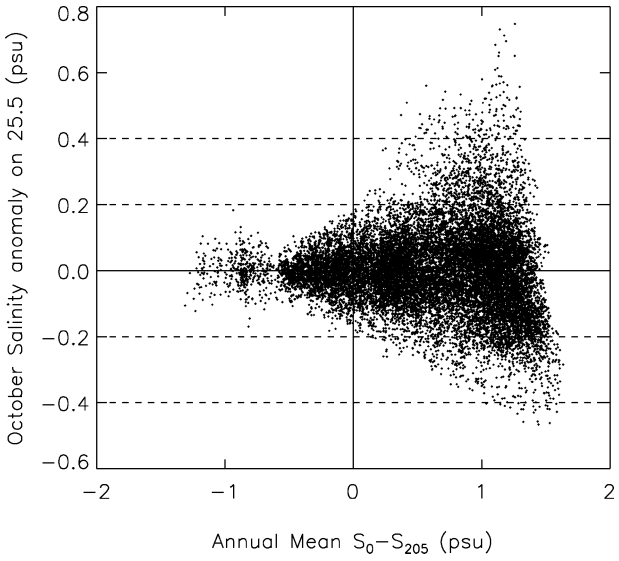

FIG. 2. Scatterplot showing the relation between the annual mean upper-ocean salinity gradient defined as $S(0\text{ m}) - S(205\text{ m})$ and the postmixing (Oct) salinity anomaly on the surface $\sigma_0 = 25.5$. Each point represents a single horizontal grid location in the box 45°–15°S, 240°–290°E for a given year.

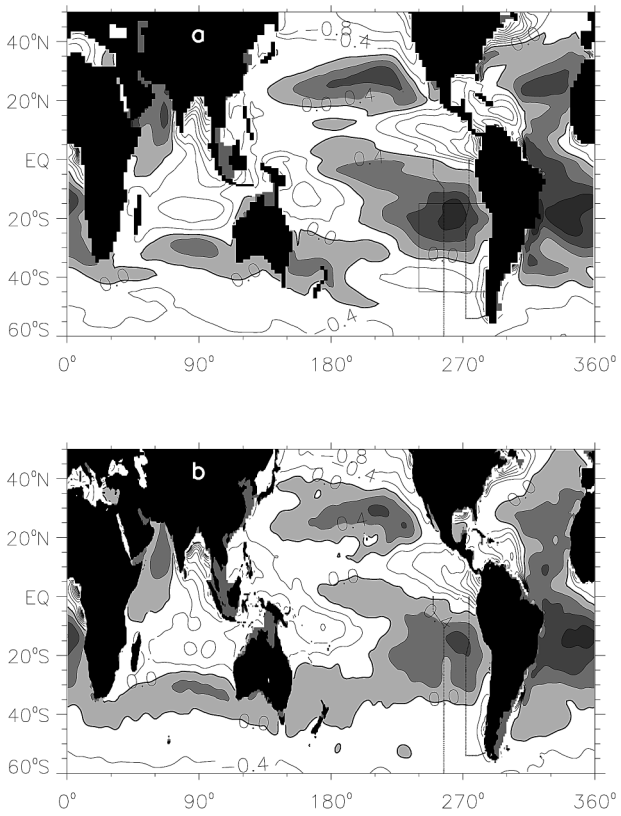

FIG. 3. (a) Spatial map of 40-yr mean $S(0\text{ m}) - S(205\text{ m})$ (psu) from the model, and (b) $S(0\text{ m}) - S(200\text{ m})$ from the *WOA98* climatology. Positive differences are shaded gray. The box outlines the region included in Fig. 2. The dotted lines indicate station locations for WOCE lines P18 (westernmost) and P19 (easternmost) used for more detailed comparisons in appendix A. The contour interval is 0.4 psu.

as will be shown in section 4. The question of isopycnal anomaly origins is twofold: 1) why are the eastern subtropics the source of such high spiciness variability on this isopycnal, and 2) what determines the magnitude and sign of significant anomaly generation in this region?

Figure 2 shows that large spiciness anomalies ($>\pm 0.2$ psu) originate exclusively where annual mean surface salinity exceeds the salinity at depth in the upper ocean, and larger vertical salinity gradients tend to be associated with larger spiciness anomalies. The Fig. 2 scatterplot incorporates all horizontal grid points in the region 45°–15°S, 240°–290°E, and all 40 yr of model integration are included. Positive values of $S(0\text{ m}) - S(205\text{ m})$ indicate that the mean near-surface water column is unstable in salinity. Since seasonal and interannual variations of $S(0\text{ m}) - S(205\text{ m})$ are relatively small in comparison with regional variations, the relationship seen in Fig. 2 has primarily geographic significance. The extreme spiciness anomalies ($>\pm 0.4$ psu) almost all originate within the source regions 1 and 2 defined in Fig. 1.

Both the model and the National Oceanographic Data Center (NODC) *World Ocean Atlas 1998* (*WOA98*; Levitus et al. 1998) show that large regions of the world ocean have a destabilizing mean upper-ocean salinity gradient (Fig. 3), with the largest gradients found between 10° and 30° latitude in both hemispheres of the Atlantic, Pacific, and Indian basins. Although the broad, global patterns between the model and the *WOA98* dataset are in quite good agreement, the model does appear to generate a larger vertical salinity gradient in the key SEP region. Factors contributing to the discrepancy, including poor sampling in the *WOA98* database, are discussed in appendix A, where a comparison with World Ocean Circulation Experiment (WOCE) hydrographic lines shows that the model does reproduce the observed upper-ocean salinity structure very well in the SEP. The sharp vertical salinity gradients at these latitudes are associated with local holes of low mean upper-ocean density stratification in the northeastern and southeastern subtropical Pacific (Fig. 4) in both the model and *WOA98*. These holes also coincide with local maxima in winter mixed layer depth (not shown), which in the Northeast Pacific has been associated with the formation of eastern subtropical mode water (Hautala and Roemmich 1998). Together, Figs. 2, 3, and 4 suggest an answer to the first question posed above regarding anomaly origins. Large vertical temperature gradients associated with high insolation result in a highly stratified upper 200 m in the Tropics throughout the year (Fig. 4). The ''spicy'' regions in the subtropical Pacific are characterized by large vertical salinity gradients that exist at latitudes where the vertical temperature gradient can strongly stabilize the water column only in summer. Winter cooling erodes the thermal stratification, allow-

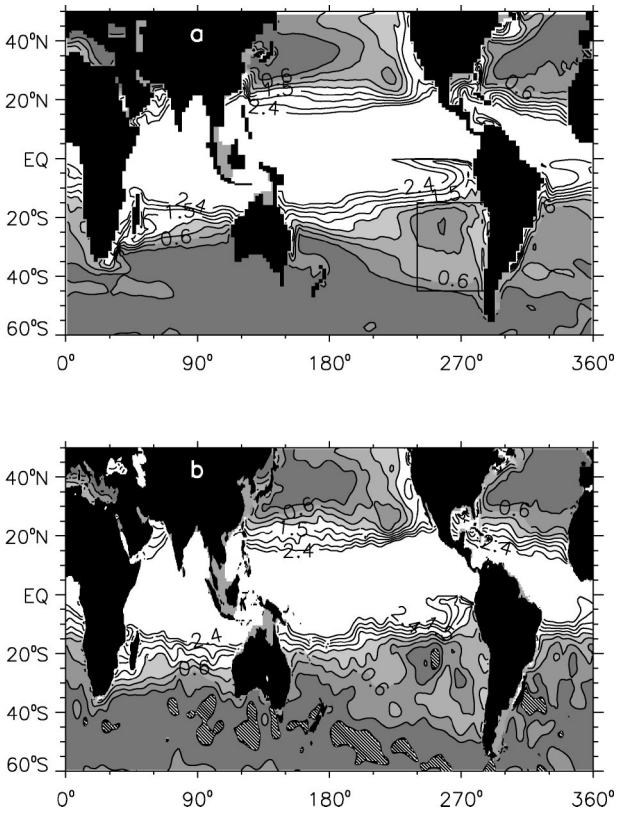

FIG. 4. (a) Spatial map of 40-yr mean winter (Mar/Sep) σ_0(205 m) − σ_0(0 m) (kg m^{-3}) from the model, and (b) σ_0(200 m) − σ_0(0 m) from the *WOA98* monthly climatology. The contours go from 0.0 to 2.4 by 0.3 kg m^{-3}; values above 2.4 kg m^{-3} exist over most of the Tropics. Differences below 1.2 kg m^{-3} are shaded gray with darker shades for smaller values (weaker stratification). Values below 0.0 in the bottom panel, indicating erroneous instability in the *WOA98* climatology, are crosshatched.

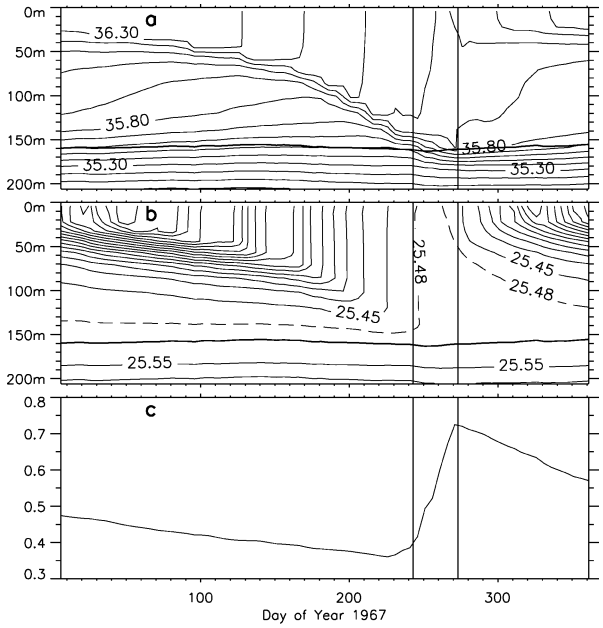

FIG. 5. Time series of 5-day mean (a) salinity (psu), (b) density (kg m^{-3}), and (c) salinity anomaly on σ_0 = 25.5 (psu), all at 23°S, 258°E during 1967. The anomaly is computed as the deviation from the 40-yr mean value on the surface. The thick black line in (a) and (b) represents the isopycnal σ_0 = 25.5. Contour intervals are 0.1 psu and 0.05 kg m^{-3} for salinity and density, respectively. An additional contour at 25.48 kg m^{-3} has been added in the density plot. Vertical lines delimit the month of Sep.

ing the salinity gradient to enhance the wind mixing and produce a deep layer of near uniform density with a wide range of temperature and salinity combinations.

An example of the evolution of upper-ocean salinity and density during a large positive anomaly injection event in 1967 is shown in Fig. 5. The grid point examined lies roughly in the middle of SEP source region 1. The upper-ocean gradient, S(0 m) − S(205 m), is greater than 1.0 psu, reaching a maximum in the summer when increased evaporation produces a large reservoir of high-salinity surface water. During austral autumn, the gradually deepening mixed layer increases the salinity at depth while concentrating the upper-ocean salinity gradient into a sharp, unstable halocline at the base of the mixed layer. The sharp, stable pycnocline associated with warm summer surface waters erodes by August, and the surface density mixes to within 0.02 kg m^{-3} of 25.5 at the acme of mixing. In September, the temperature and salinity gradients at the base of the mixed layer are almost density-compensating, and so they cross the surface σ_0 = 25.5 without affecting the depth of the isopycnal, thereby generating significant property anomalies on the isopycnal by the month of October. The salinity anomaly on the isopycnal at this location, already ≈0.4 psu before the injection event, grows to ≈0.7 psu before the pycnocline begins to reform. A key feature of winter mixing in this region evident in Fig. 5 is the existence of a sharp halocline/thermocline at the base of the mixed layer, which is largely transparent in density.

The winter erosion of near-surface density layers in a water column characterized by a large, destabilizing vertical salinity gradient can result in a column profile which is nearly parallel to isopleths of density in temperature–salinity space. For such water columns, a small change in the slope of the profile can result in large positive spiciness anomalies on a small band of density surfaces. Figure 6 shows the evolution in T–S space of the upper-ocean water column at the point examined above during the positive anomaly injection event of 1967. In March, the summer density stratification is evident above ≈100 m, while the deeper water is almost uniform in density. By September, the surface stratification has collapsed and mixing below the layer of well-mixed temperature and salinity produces a further alignment of the column along the σ_0 = 25.5 isopleth. The salinity gradient between the surface and the deeper water is largely preserved but tightens sharply above the 181-m model grid level, as seen in Fig. 5. The intersection of the water column with the σ_0 = 25.5 sur-

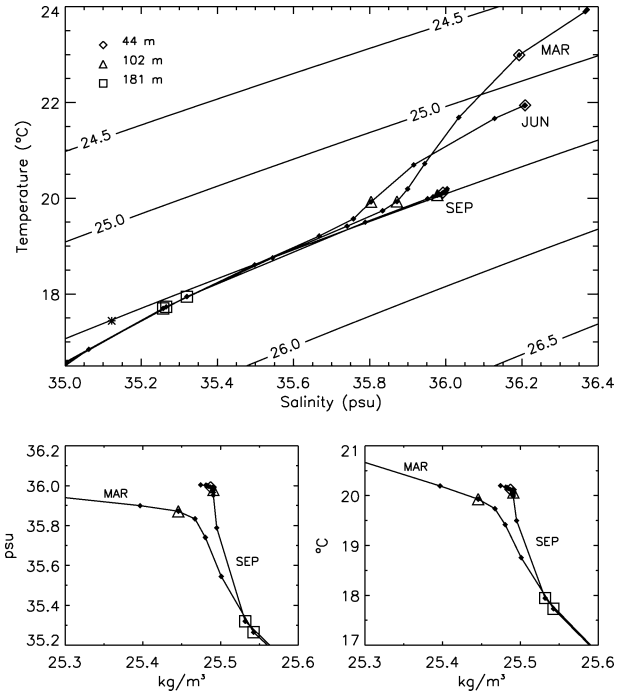

FIG. 6. Evolution of the upper-ocean water column at 23°S, 258°E from Mar to Sep 1967. Filled diamonds represent model depth levels. The asterisk in the upper plot indicates the 40-yr mean temperature and salinity on $\sigma_0 = 25.5$ at this location. The lower plots show blowups in (lower left) salinity–density and (lower right) temperature–density coordinates of the difference between the Mar and Sep water columns.

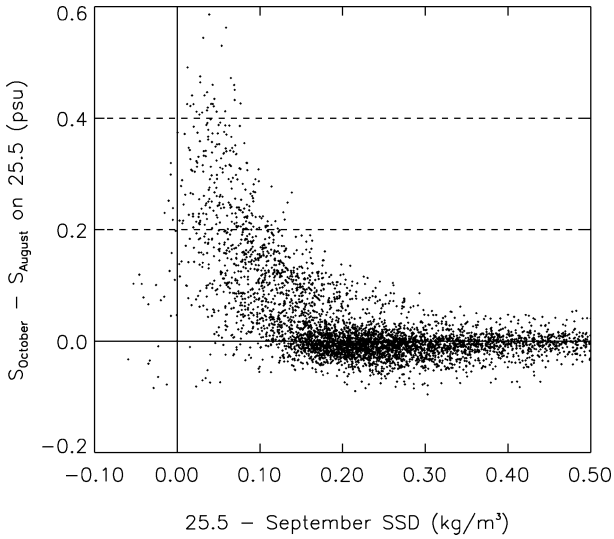

FIG. 7. Scatterplot showing the relation between the difference between 25.5 kg m^{-3} and the Sep sea surface density and the winter anomaly injection, defined as the difference of Oct and Aug salinities on $\sigma_0 = 25.5$. Only model grid points within source regions 1 and 2 are included.

face jumps abruptly to a significantly higher temperature–salinity combination, resulting in the sudden positive spiciness pulse on the isopycnal seen in September of Fig. 5. The spiciness injection that occurs in a thin density band around 25.5 kg m^{-3} is easier to see when the column profile is plotted in salinity–density and temperature–density space, as shown in the lower panels of Fig. 6. These plots show that the late-winter increase in salinity and temperature occurs over a density range of $\approx$0.05 kg m^{-3}. The robust injection event examined in detail in Fig. 5 and 6 is characteristic of positive anomaly events that occur on $\sigma_0 = 25.5$ throughout the SEP formation region in winter.

In the SEP region, sharp increases in salinity between August and October occur regularly on subducted isopycnals that are positioned just below the base of the mixed layer and which are therefore only slightly denser than the winter sea surface density. Figure 7 shows that for the isopycnal $\sigma_0 = 25.5$, winter injections of spiciness in source regions 1 and 2 are associated with midwinter sea surface densities within $\approx$0.1 kg m^{-3} of the isopycnal density. In other words, anomaly injection events on $\sigma_0 = 25.5$ are associated with winter mixing that brings the isopycnal to the brink of outcropping. In order to be plotted in Fig. 7, the isopycnal $\sigma_0 = 25.5$ had to exist (in the monthly mean) at a given location in both August and October. A positive abscissa value further implies existence in September as well. Negative abscissa values are all from source region 2 and indicate that the isopycnal outcropped in September. The fact that almost all large winter salinity injections on $\sigma_0 = 25.5$, in both source regions 1 and 2, occur at locations where the isopycnal exists throughout the winter (positive abscissa values; no outcropping) implies that the same subsurface process is at work in both regions, even though the outcrop tends to fall much nearer to anomaly injection points in source region 2 than in source region 1. Negative anomalies tend to grow in the absence of such injection events, when September stratification between the isopycnal and the sea surface remains relatively large.

As a water column becomes parallel to density isopleths in temperature–salinity space, it becomes inherently spicy and is characterized by a density ratio $R_\rho \rightarrow 1$, where

$$R_\rho = \alpha \partial_z T / (\beta \partial_z S). \quad (4)$$

In (4), α and β are the coefficients of thermal expansion and haline contraction, respectively. The mean September value of this ratio on the surface $\sigma_0 = 25.5$ is a strong indicator of the sign and magnitude of postmixing salinity anomalies on the isopycnal in the formation region under investigation (Fig. 8). Large, positive spiciness anomalies are generated in source regions 1 and 2 when R_ρ is less than $\approx$1.5, and values of R_ρ closer to 1.0 result in more positive anomalies. Negative anomalies are associated with higher R_ρ values. Source regions 1 and 2 are characterized by habitually low winter R_ρ on the isopycnal $\sigma_0 = 25.5$, and interannual variations about this low mean determine the sign of anomalies. Values of R_ρ less than about 2.0 are associated

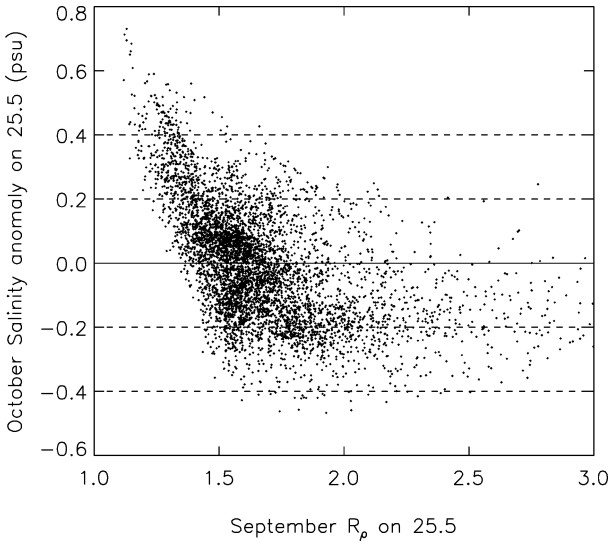

FIG. 8. Scatterplot showing the relation between the Sep value of R_ρ on $\sigma_0 = 25.5$ and the postmixing (Oct) salinity anomaly on $\sigma_0 = 25.5$. Only model grid points within source regions 1 and 2 are included.

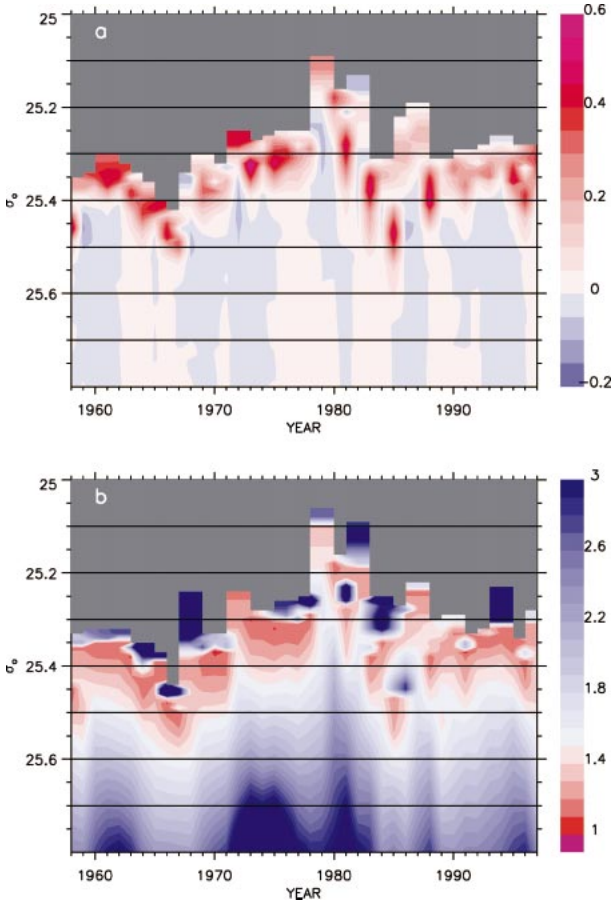

FIG. 9. (a) Winter salinity injection (psu), defined as the difference of Oct and Aug mean isopycnal salinity, at the model grid point 23°S, 258°E plotted as a function of year and density; and (b) Sep mean R_ρ at the same location. Gray shade indicates that the density value did not exist at the point in the monthly mean needed for the plot.

with enhanced mixing due to double diffusive processes (Schmitt 1981), which are absent in this model integration. Branch run experiments that use reasonable estimates for double diffusion mixing coefficients (St. Laurent and Schmitt 1999) show some effect on the phasing and sharpness of injection events but little effect on the magnitude of anomalies (see appendix B on vertical mixing sensitivity).

The R_ρ values near unity at the base of the mixed layer are the regular result of winter mixing in this region, and so changes in the density structure of the upper-ocean water column are what account for interannual spiciness variability on any given isopycnal. Figure 9 refocuses attention on the grid point at 23°S, 258°E examined in Figs. 5 and 6. A yearly time series of winter salinity injection reveals that positive injections exceeding ≈0.2 psu take place regularly on density surfaces just below the winter sea surface density, at the base of the mixed layer where $R_\rho \to 1$. The $\sigma_0 = 25.5$ surface experiences three main episodes of $R_\rho \to 1$ during the 40-yr integration (1958–59, 1965–68, and 1985), and, we will show, this can explain the emergence of three major positive spiciness signals emanating from the SEP region on the surface $\sigma_0 = 25.5$. Likewise, a large negative anomaly growth on this isopycnal in the mid 1970s can be related to the decade-long shift of wintertime injections to slightly lower densities (≈25.32, Fig. 9).

Although observations from the SEP region in winter are scarce, at least one hydrographic profile from the World Ocean Database 2001 (Conkright et al. 2002) taken in mid-September of 1967 at 14.9°S, 271.7°E shows evidence of R_ρ values very close to 1 in a column of water ≈40 m thick just below the mixed layer (Fig. 10). A recent analysis of WOCE meridional hydrographic sections P18 and P19, which transect the SEP region between January and April along 103° and 88°W, respectively, reveals the existence of a large lens of water with $R_\rho < 2$ located ≈33°–15°S between the surfaces $\sigma_0 = 25.0$ and $\sigma_0 = 25.6$, the suggested density boundaries of South Pacific Eastern Subtropical Mode Water (Wong and Johnson 2003). Also, Tsuchiya and Talley (1998) used CTD profiles taken at 88°W to show that salt fingering (implied by $R_\rho < 2$) on $\sigma_0 \approx 25.5$ is likely to be especially active between 30° and 20°S. Although these sections were not from winter months, the data support the model finding that $R_\rho \to 1$, reaching a minimum in winter, is characteristic of water columns in this region of the Pacific.

Negative anomalies on $\sigma_0 = 25.5$ can be attributed to the slow, steady, cumulative effect of advective processes working in the absence of injection events. A large negative anomaly emanating from the SEP region in the early 1970s (see section 5) grows steadily throughout the year 1972 at the grid point 23°S, 258°E

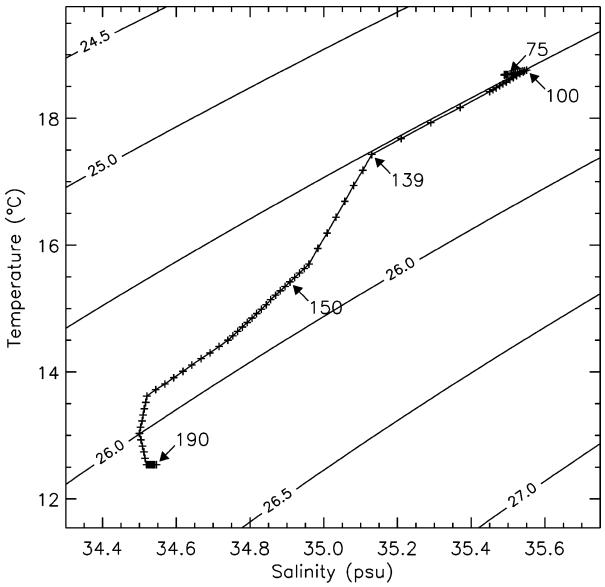

FIG. 10. CTD profile from the World Ocean Database 2001 taken on 11 Sep 1967 at the South Pacific location 14.9°S, 271.7°E shows $R_\rho \rightarrow 1$ in a layer of water ≈40 m thick at the base of the mixed layer. Depth in meters is indicated with arrows.

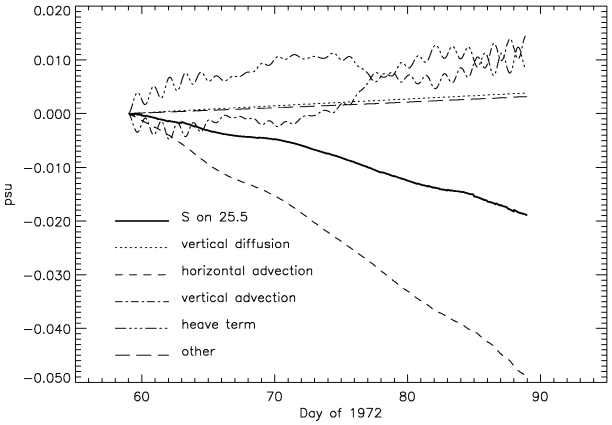

FIG. 11. Salinity budget on $\sigma_0 = 25.5$ at the model grid point 23°S, 258°E during Mar 1972, when isopycnal salinity is trending steadily lower.

examined in Figs. 5, 6, and 9. In that year, $\sigma_0 = 25.5$ remains well-insulated in density from the winter mixed layer, and no winter pulse interrupts the steady downward trend in salinity (Fig. 9). A monthlong decomposition of salinity tendency terms at this point [see Eq. (3)] reveals that horizontal advection is driving the negative trend in isopycnal salinity (Fig. 11). The vertical diffusion term, which accounts almost entirely for the dramatic September 1967 salinity increase, has only a minor positive effect. The heave correction term cancels the inertial oscillations evident in the vertical advection term, leaving no trace of high-frequency variation on the isopycnal, and together they reduce by about 1/2 the negative tendency of the horizontal advection term. The mean horizontal circulation in the SEP region flows generally northward across a mean salinity gradient on the isopycnal (not shown), bringing in colder, fresher water from the Southern Ocean and driving a steady negative trend in salinity on $\sigma_0 = 25.5$ throughout the region. Periods of extended insulation from the winter mixed layer can then result in large negative anomaly growth. The existence of a mechanism (horizontal advection) working to counter the effects of positive winter anomaly events (vertical diffusion) contributes to the high variance seen on this surface in the SEP region.

4. Anomaly propagation

Figure 1 and isopycnic depth contours (not shown) suggest equatorward and westward advection of salinity variance on $\sigma_0 = 25.5$ from SEP source regions 1 and 2, and from the eastern subtropics of the North Pacific (NEP). Furthermore, this variance is not transmitted directly to the equator, but rather to the western boundaries at ≈12°N and ≈7°S. These latitudes are probably close to the bifurcation points that distinguish recirculation pathways that turn poleward at the western boundary from the equatorial exchange pathways that turn equatorward at the western boundary (Liu et al. 1994; Rothstein et al. 1998; Harper 2000). Therefore, there may be both recirculating and equatorial exchange subduction pathways emanating from the SEP and NEP formation regions, which diverge at the western boundary and make tracking anomalies beyond the gyre interior problematic. The local variance maximum on the equator at ≈140° in the western Pacific could result from either a constructive convergence or a focusing of anomalies arriving from either hemisphere along equatorward pathways, or a local generation process could be contributing or even dominating.

To track the propagation of annual anomalies, we have defined a pair of northern and southern variance pathways that follow the lobes of maximum salinity variance shown in Fig. 1. The pathways follow the crests of rms salinity westward and equatorward, starting at or near the locations of peak rms in the eastern subtropics (30°N, 229°E; 21°S, 258°E). In the tropical western Pacific, where the rms salinity pattern is less well-defined, the pathways follow vectors of mean horizontal velocity on the isopycnal (not shown). Like source region 2 of the SEP, there is a secondary rms maximum in the eastern subtropics of the North Pacific (NEP), whose variance envelope connects with the larger and stronger lobe, such that the following static pathway analysis only partially reflects the full signal generation and evolution.

Figure 12 shows the annual mean salinity anomaly computed along the paths on the surface $\sigma_0 = 25.5$ for each year of the integration. There is clear evidence that spiciness signals originating in the eastern subtropics of both hemispheres propagate westward to the boundary and then, at least partially, equatorward to a conver-

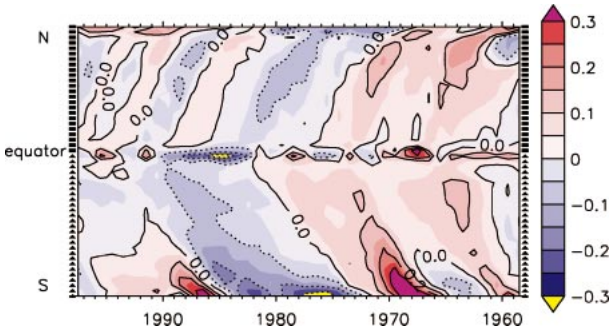

FIG. 12. Propagation of salinity anomalies computed as annual deviations from the mean isopycnal salinity at the horizontal pathway locations shown in Fig. 1. The path markers are oriented southernmost to northernmost on the *y* axis, while model forcing year runs from right to left on the *x* axis. Contours are 0, ±0.1, ±0.2, and ±0.3 psu. A corresponding plot exists for temperature (not shown).

gence in the western equatorial Pacific. The SEP origin is more robust than its NEP counterpart on this isopycnal, but perhaps not on lower-density isopycnals (section 5). The southern pathway is dominated by a large positive spiciness anomaly in the late 1960s that propagates directly into the interior followed by a period of large negative anomaly growth in the late 1970s that begins to move in the early 1980s. Positive signals originating in the late 1950s and late 1980s are relatively weak. The start of the SEP pathway is near the grid point examined in Figs. 5, 6, 9, and 11, and a comparison of Figs. 12 and 9 shows that low R_ρ winter salinity injections can explain the three large positive spiciness signals emanating from the SEP source and effecting decadal change in the South Pacific thermocline. The choice of $\sigma_0 = 25.5$ is not optimal in the north, where the evolution of spiciness signals is more complex. Anomalies do not propagate as cleanly from the region of maximum variance into the interior and in some years appear to gain strength south of ≈20°N. This is perhaps related to a convergence near this latitude of the main lobe with spiciness variance originating from a region off the west coast of Mexico (Fig. 1), and it is also possible that $\sigma_0 = 25.5$ is gaining variance through diapycnal mixing.

The spatial evolution of Southern Hemisphere spiciness anomalies during a 9-yr period is shown in Fig. 13. The interval 1966–74 captures the largest salinity anomaly generated on this isopycnal over the 40-yr period of the hindcast. In 1967, preexisting positive anomalies are intensified during late winter in both SEP source regions 1 and 2. The anomaly in source region 1 is significantly displaced from the winter outcrop of the isopycnal, and its origin has been detailed above for an example grid point. After reaching the western equatorial Pacific around 1973, there is some evidence that the signal continues rapidly eastward along the equator in 1974. A positive 1970–71 anomaly from source region 2 subducts and moves onto the pathway defined above, but a positive 1973–74 anomaly formed in source region 2 is held in check by a negative anomaly developing in source region 1. The existence of competing subducted anomalies in 1974 might explain why the negative anomaly of the mid-1970s does not proceed along the southern pathway until the early 1980s in Fig. 12.

Although not a focus of the current study, eastward propagation of salinity anomalies along the equator is evident in Fig. 13. One event begins in the west in 1966 and another in 1973. Despite the limitations of the pathway analysis, Fig. 12 does suggest that, in both of these years, constructive convergence of anomalies originating years earlier in the subtropics of both hemispheres is a contributing source. However, Fig. 12 also shows examples of what might be destructive convergence in 1990, a focusing or amplification of a negative anomaly from the north in 1984 and of a positive anomaly from the south in 1978, and local generation of a positive anomaly in 1991.

5. Discussion

Positive winter anomaly genesis on $\sigma_0 = 25.5$ in the SEP region of the model correlates weakly with collocated atmospheric fluxes. Thus, we were not able to explain the origins of the large Southern Hemisphere anomalies in the model in terms of direct atmospheric coupling; a result consistent with observational studies (e.g., Kessler 1999). Instead, positive anomalies in the SEP are generated by diapycnal mixing across subducted isopycnals, while negative anomalies accumulate via isopycnal advection (section 3). As with all modeling studies, these results depend on the fidelity of the model solutions. The credibility of these mechanisms of spiciness generation is supported by the fact that the diapycnal mixing scheme (KPP) is well tested, though not yet in these exact circumstances, the model reproduces a realistic background state (appendix A) implying reasonable mean forcing and ocean dynamics, and the characteristic low R_ρ signature is consistent with the limited observations from this region (e.g., Fig. 10 and appendix A; Tsuchiya and Talley 1998; Wong and Johnson 2003).

The subsurface processes responsible for spiciness generation on $\sigma_0 = 25.5$ in a column of SEP water (vertical diffusion and horizontal advection) are influenced, but not set, by local surface forcing. A related result is that the decadal variability of anomalies on $\sigma_0 = 25.5$, evident in Figs. 9 and 12, correlates negligibly with large-scale climate variations over the SEP formation region. What then modulates the magnitude of winter injection events on $\sigma_0 = 25.5$ on these time scales? Or, following from section 4, what is responsible for the decadal variation in upper-ocean density stratification of the SEP region? Figure 14 illustrates the nonlocal atmospheric forcing that, we postulate, is at least partly responsible for the decadal evolution of anomalies on $\sigma_0 = 25.5$. It suggests that the magnitude

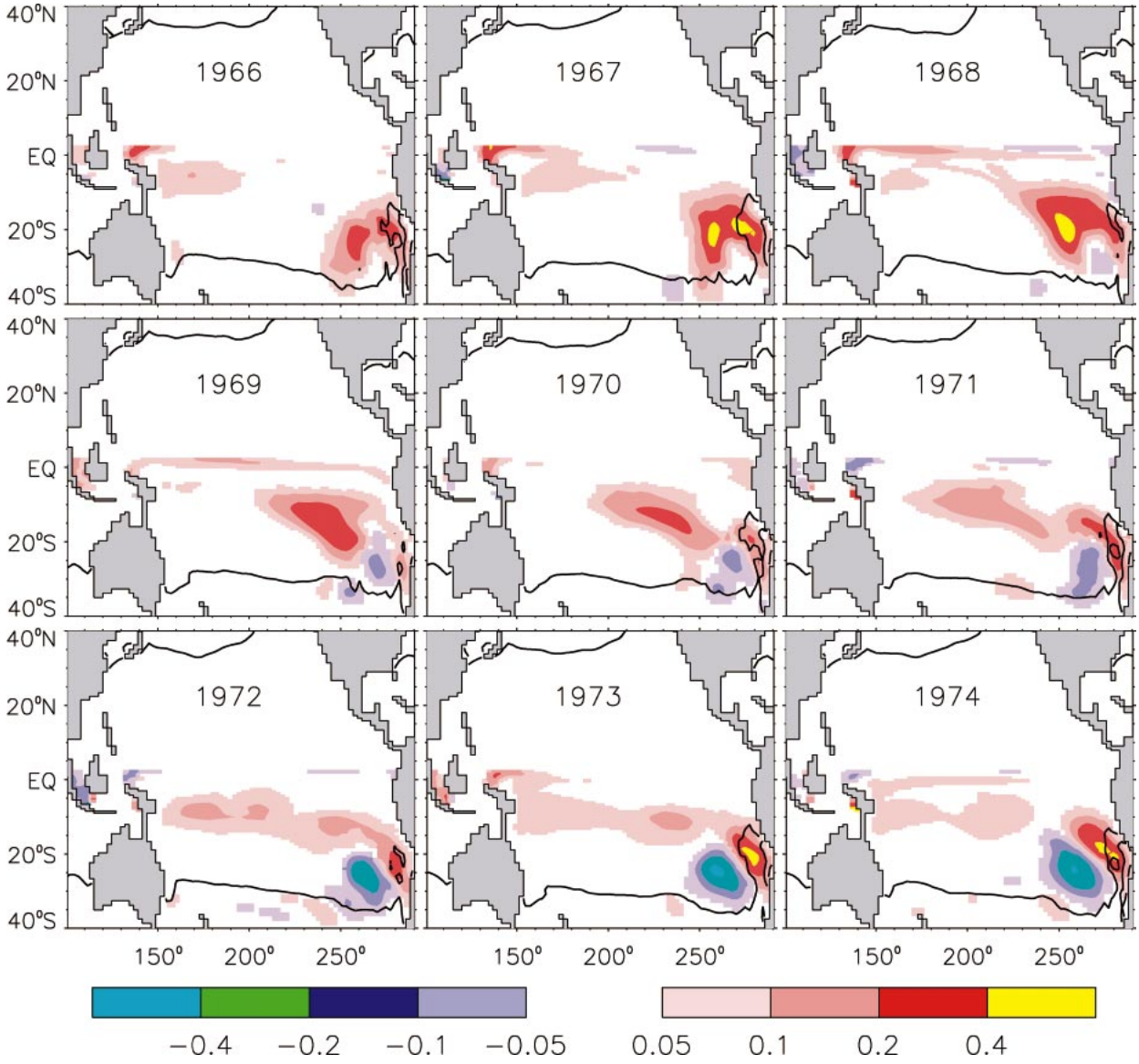

FIG. 13. Example of the spatiotemporal evolution of Southern Hemisphere anomalies on $\sigma_0 = 25.5$. Each panel shows the annual mean anomaly of isopycnal salinity from the 40-yr mean. For clarity, only anomalies of magnitude ≥0.05 psu and south of 4°N are plotted. The contour line shows the position of the winter (mean Mar/Sep) surface outcrop of the isopycnal for that year.

of the unstable vertical salinity gradient in the anomaly formation region is related to the integral salinity gain of near-surface water parcels transported by prevailing surface currents through subtropical evaporation zones. The accretion and depletion of the SEP surface salinity reservoir, set by ocean advection time scales, may contribute to the decadal nature of variability on $\sigma_0 = 25.5$.

The relationships between local and nonlocal surface forcing and specific isopycnal spiciness changes appear to be exceedingly complex, which places rigorous demands on the hindcast. A particular concern is that only the NCEP forcing that gives the wind stress and turbulent heat fluxes varies over the full 40 yr. These fluxes do dominate the interannual variability of the mechanical and heat forcing, but not of the freshwater forcing, which has a large contribution from year-to-year precipitation changes. Fortunately, the use of a climatological seasonal cycle of precipitation prior to 1979 is less consequential in the net evaporation zones of Fig. 14, where all datasets indicate consistently low precipitation.

A strong subtropical–tropical link exists in the model, which advects the subsurface-generated decadal spiciness anomalies to the western boundary of the Pacific on time scales of 6–10 yr. The magnitude of downstream signals in Fig. 12 is not inconsistent with Kessler's (1999) finding of a 1987–96 range of salinity of ≈0.4 psu on $\sigma_0 = 24.5$ at 3° − 5°S, 180°. The southern

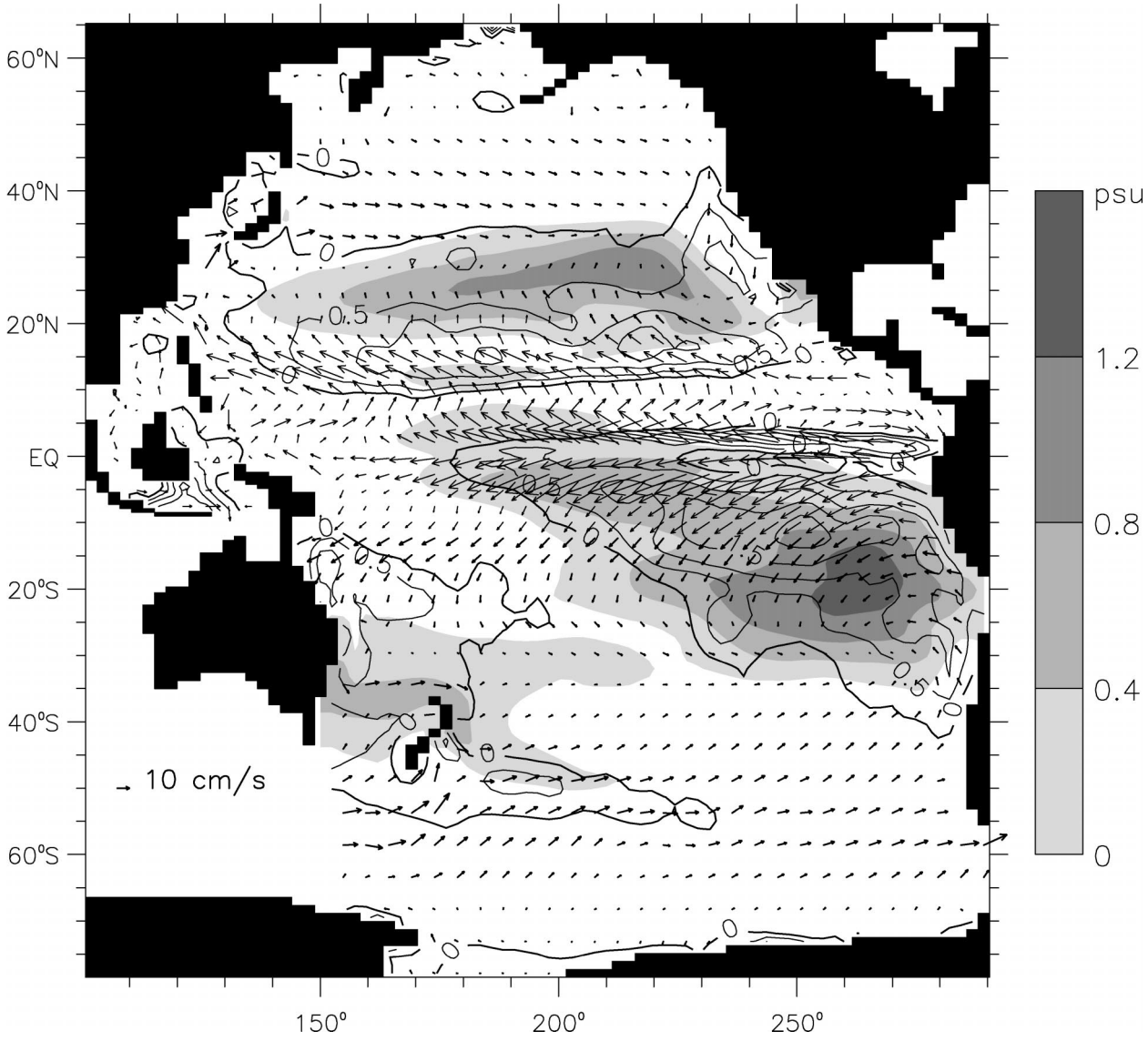

FIG. 14. Pacific 40-yr mean upper-ocean salinity gradient $S(0\text{ m}) - S(205\text{ m})$ (psu; shaded where positive) overlayed with contours of surface salt flux (10^{-7} msu cm s^{-1}; contoured where positive). Forty-year mean ocean surface velocity vectors are also overlaid. Regions where $S(0\text{ m}) - S(205\text{ m})$ is positive and large are significantly displaced from high salt flux zones in a manner that suggests that the largest gradients are related to the longest surface parcel pathlengths through evaporative zones.

pathway shows a salinity range of only ≈0.2 psu at 180°. The persistance of isopycnal anomalies in the model is largely determined by the value of the Redi diffusion, set to $K_R = 800\ \text{m}^2\ \text{s}^{-1}$, but is marked by considerable uncertainty. Tuning this parameter to obtain a better correspondence with downstream observations would make sense only if future observations confirm the realism of model anomalies in the SEP source regions. The equatorial links suggested by Figs. 12 and 13 may not represent reality, because they depend on the overall general circulation of the Pacific, which is sensitive to many model parameters including the resolution and the large scale forcing. Slight changes could transform the maximum spiciness variance pathway from one characterized predominantly by equatorial exchange to one that is largely recirculating, or vice versa, with potential implications for the role of advected spice anomalies in decadal equatorial variability.

The spiciness formation zone characteristics that we have identified are not unique to the Pacific basin, and conditions similar to those that lead to anomaly generation on $\sigma_0 = 25.5$ in the SEP region might account for high isopycnal variability in other regions of the ocean. Based on section 3, significant interannual spiciness variability is expected wherever large unstable salinity gradients are present in conjunction with weak stratification and strong mixing in winter. The telltale signature should be $R_\rho \to 1$ in the upper pycnocline.

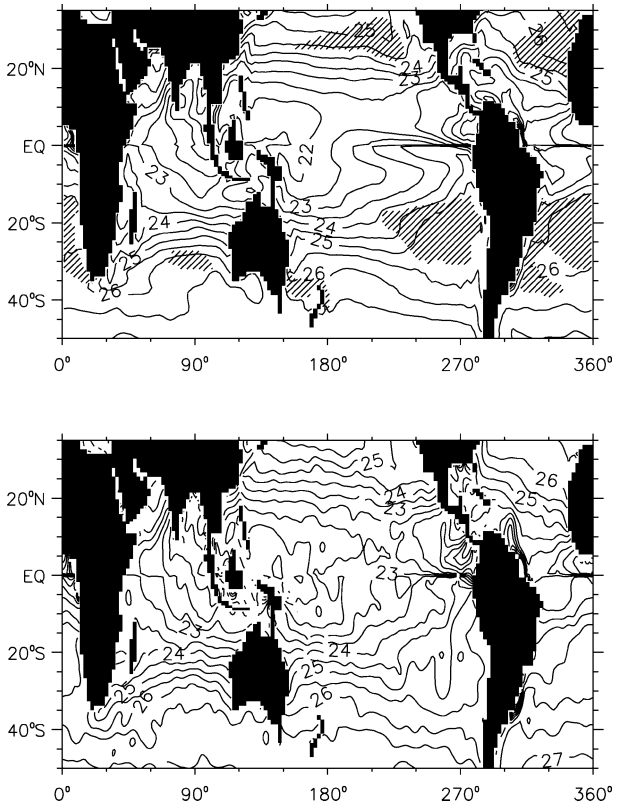

FIG. 15. Mean winter (Mar/Sep) sea surface density (kg m^{-3}) from the (top) model and the (bottom) *WOA98* climatology. The overlay in the top panel indicates regions expected to be conducive to wintertime pulses of positive spiciness through generation of $R_\rho \rightarrow 1$ in the upper 200 m; crosshatched areas show where Mar/Sep mean $\sigma_0(205\text{ m}) - \sigma_0(0\text{ m}) < 1.2$ kg m^{-3} and annual mean $S(0\text{ m}) - S(205\text{ m}) > 0.4$ psu (cf. Figs. 3 and 4).

Figure 15 shows that such zones exist in each of the ocean basins. The exceptionally high variability on $\sigma_0 = 25.5$ in the SEP region appears to be related to the fact that this surface subducts under a large body of highly uniform density water, which is prone to low winter R_ρ. This particular density surface is high enough to outcrop poleward of the SEP region of low winter R_ρ while low enough to occasionally approach the sea surface density, so that large winter injections of high temperature and salinity can occur. Confidence in this result is increased by the Fig. 15 comparison of winter surface density from *WOA98* climatology. Most notably, the area of the South Pacific east of 220°E and bounded by the $\sigma_0 = 24.5$ and $\sigma_0 = 25.5$ contours is about the same size and in very much the same location. Over this area, the surface density differences, including the position of the $\sigma_0 = 25.5$ contour, are within the uncertainty of the *WOA98* database and processing (appendix A; see also unstable regions of Fig. 4).

A close analog to $\sigma_0 = 25.5$ in the SEP region is $\sigma_0 = 26.0$ in the South Atlantic, which appears well-positioned relative to a very large formation region stretching all the way from South America to Africa. The formation zone in the North Atlantic is comparable in size to that in the SEP but covers a broader range of isopycnal outcrops and so presents a more limited area to any particular density surface. Similar regions in the North Pacific, south Indian, and Tasman Sea regions are smaller in area. A measure of the capacity of spiciness generation, the maximum absolute yearly anomaly from the 40-yr mean isopycnal salinity, is plotted on a range of density surfaces in Fig. 16, for comparison with Fig. 15. The formation zones, defined in Fig. 15 on the basis of weak winter stratification paired with destabilizing upper-ocean salinity gradient, do show some success in identifying the geographic distribution of significant variability on the surfaces of Fig. 16. In the North Pacific, $\sigma_0 = 25.0$ is poleward of much of the formation zone (Fig. 15) and has large anomalies in Fig. 16. Similar correspondences are found on $\sigma_0 = 25.5$ in the SEP and to a lesser extent the North Pacific, $\sigma_0 = 26.0$ in the South Atlantic, and $\sigma_0 = 26.5$ in the North Atlantic and south Indian oceans. All surfaces in Fig. 16 show large anomalies off Argentina, but these are likely due to variability in the modeled Malvinas Confluence. The apparent weakness of the Northern Hemisphere pathway in comparison with the Southern Hemisphere on $\sigma_0 = 25.5$, evident in Figs. 1 and 12, can be attributed to the fact that the formation zone in the northeastern Pacific operates more efficiently on slightly lower density isopycnals (closer to 25.0). The surface $\sigma_0 = 25.5$ was chosen for special consideration on the basis of exceptionally strong South Pacific signals.

The propagation of spiciness anomalies through basin interiors, evident in Fig. 16 in both Pacific hemispheres on $\sigma_0 = 25.5$, may also be occurring on $\sigma_0 = 26.0$ from the mid–South Atlantic to the equator following the Brazilian coast, and possibly on $\sigma_0 = 26.5$ from the eastern south Indian region to Madagascar or from northwestern Africa to the equatorial Atlantic. It may be possible, in various regions of the World Ocean, to trace deep variability on particular isopycnals to spiciness formation zones where winter mixing processes generate R_ρ near 1 on those isopycnals.

The zones identified in Fig. 15 as sites of potentially significant interannual spiciness generation overlap mode water formation regions, which have been identified in the North Atlantic (Siedler et al. 1987), South Atlantic (Provost et al. 1999), North Pacific (Hautala and Roemmich 1998), southwestern Pacific (Roemmich and Cornuelle 1992), and southeastern Pacific (Wong and Johnson 2003). The subtropical regions where compensating vertical temperature and salinity gradients produce a minimal vertical density gradient, with low density ratios at the base of the mixed layer in winter, are also regions of significant pycnostad formation. Our analysis suggests that the highest variance is likely to occur on isopycnals at the high end of the range of densities defining a particular mode water, those which are only intermittently subject to salinity pulses from a mixed layer occupied by middensity mode water.

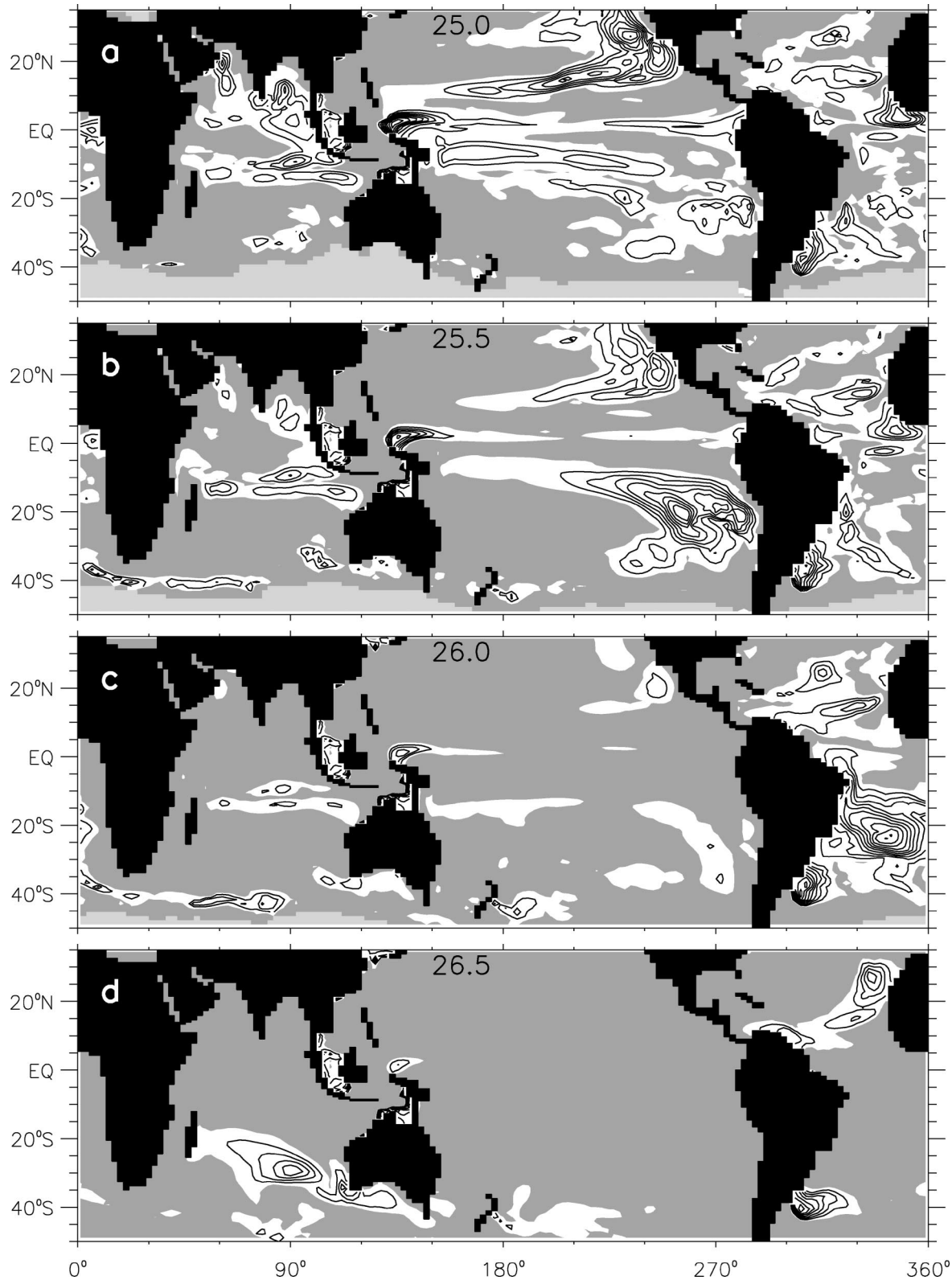

FIG. 16. Maximum absolute annual salinity anomaly (psu) from the 40-yr mean on the isopycnal surface (a) σ_0 = 25.0, (b) σ_0 = 25.5, (c) σ_0 = 26.0, and (d) σ_0 = 26.5. Contour interval is 0.05 psu. Values less than 0.1 psu are shaded gray, and outcrop regions are shaded light gray; the first contour line is 0.15 psu.

6. Summary

An OGCM hindcast of isopycnic variability during the period 1958–97 reveals that the largest interannual spiciness anomalies are not formed where an isopycnal outcrops. A region of particular interest is the subtropical southeast Pacific, where the largest interannual variability of isopycnal salinity anywhere is found on $\sigma_0 = 25.5$, and where the paucity of observations places a premium on modeling studies. In this region, spice anomalies are generated subsurface when a destabilizing salinity gradient becomes focused at the base of the mixed layer because of late winter mixing and diffuses across a nearly outcropped density surface, such that the mixing of density is deeper than that of temperature and salinity. The net result is a positive pulse of these tracers on the already subducted isopycnal surface. The spiciness formation zones where such mixing occurs are characterized by a large upper-ocean salinity inversion and weak density stratification in winter, which together result in R_ρ values that approach 1. The high variance on $\sigma_0 = 25.5$, however, also derives from the fact that the diapycnal mixing associated with these winter injections is balanced by periods of quiescence during which mean advection steadily generates anomalies of the opposite sign, with about one-half of this advection offset by vertical advection and heave.

The role of surface forcing in generating these spiciness anomalies appears to be complex, made even more so by the fact that positive and negative anomalies are produced by different processes. Variability in the unstable salinity gradient is primarily due to changes in surface salinity, which in turn depend on a combination of nonlocal evaporation and ocean surface transport, which are both affected by atmospheric circulation. It is the local surface cooling that erodes the temperature stratification in winter and the local wind stress that provides additional energy to mix the density field into the pycnocline. The advection of relatively fresh water along the isopycnal is a feature of the general circulation of the ocean basin and as such depends on the basinwide forcing, water mass formation and transformation, and ocean dynamics. Therefore, it is not surprising to find insignificant correlations between interannual variability on $\sigma_0 = 25.5$ and climate variations in the vicinity of either the anomaly generation or the isopycnal winter outcrop.

In each of the world's ocean basins there are regions of high interannual variability on select isopycnal surfaces, which appear to be analogous to $\sigma_0 = 25.5$ in the South Pacific. Their characteristics are consistent with isopycnals subducting at higher latitudes, passing underneath spiciness formation zones in winter and receiving large, density-compensating increases in temperature and salinity. However, the largest positive spice anomalies appear on different isopycnals: $\sigma_0 = 25.0$ in the northeast Pacific, $\sigma_0 = 25.5$ in the southeast Pacific, $\sigma_0 = 26.0$ in the South Atlantic, and $\sigma_0 = 26.5$ in the south Indian and North Atlantic.

On $\sigma_0 = 25.5$ in the Pacific, spiciness anomalies generated subsurface in the eastern subtropics of both hemispheres propagate as expected along geostrophic pathways toward the western Pacific, remaining as large as ± 0.2°C and ± 0.1 psu upon reaching the western boundary. There is some indication in the model that these spiciness variance pathways then connect to the equator, where they combine in some way and then propagate back toward the east.

The major model issue is the surface forcing, which required somewhat subjective corrections to near surface humidity and insolation. The lack of river runoff and uncertainties in precipitation necessitated a weak restoring to surface salinity and a spinup procedure that determined a model-dependent increase in the precipitation by a uniform factor of about 1.11. Although turbulent heat, momentum, and evaporation fluxes varied over the entire 40-yr hindcast, precipitation varied for less than 20 yr and radiation for less than 10. The most important model physics for the present study is the vertical mixing, which utilizes a well-tested parameterization that shows little sensitivity to increased vertical resolution or double diffusion. Less of an issue is the horizontal resolution, because the parameterized eddies should be adequate and the low anisotropic viscosity permits relatively realistic ocean currents to develop. Despite these potential problems, there are no serious discrepancies with existing observations, at least in the SEP. Considering all the limitations of the hindcast, we have most confidence in the model's mechanism for generating positive spice anomalies in late winter in regions of unstable salinity gradients and weak winter stratification. There is less confidence in precisely which winters these will occur and which isopycnals will be most affected. Also uncertain are the strength and geographical extent of newly formed spice anomalies and the origins of significant negative isopycnal anomalies (Fig. 11), because the datasets to test these model results do not yet exist.

Acknowledgments. The authors thank James McWilliams for helpful comments and discussion. This work has been supported by NOAA Grant NA06GP0428.

APPENDIX A

SEP Comparison with Observations

This appendix addresses the issue of model fidelity with regard to the mean upper-ocean state in which SEP winter mixing occurs. A search for hydrographic data yielded no September salinity observations within 500 km of the maximum unstable salinity gradient near 20°S in Fig. 3. The closest CTD cast (Fig. 10) was taken in 1967 around 15°S. Background salinity conditions can

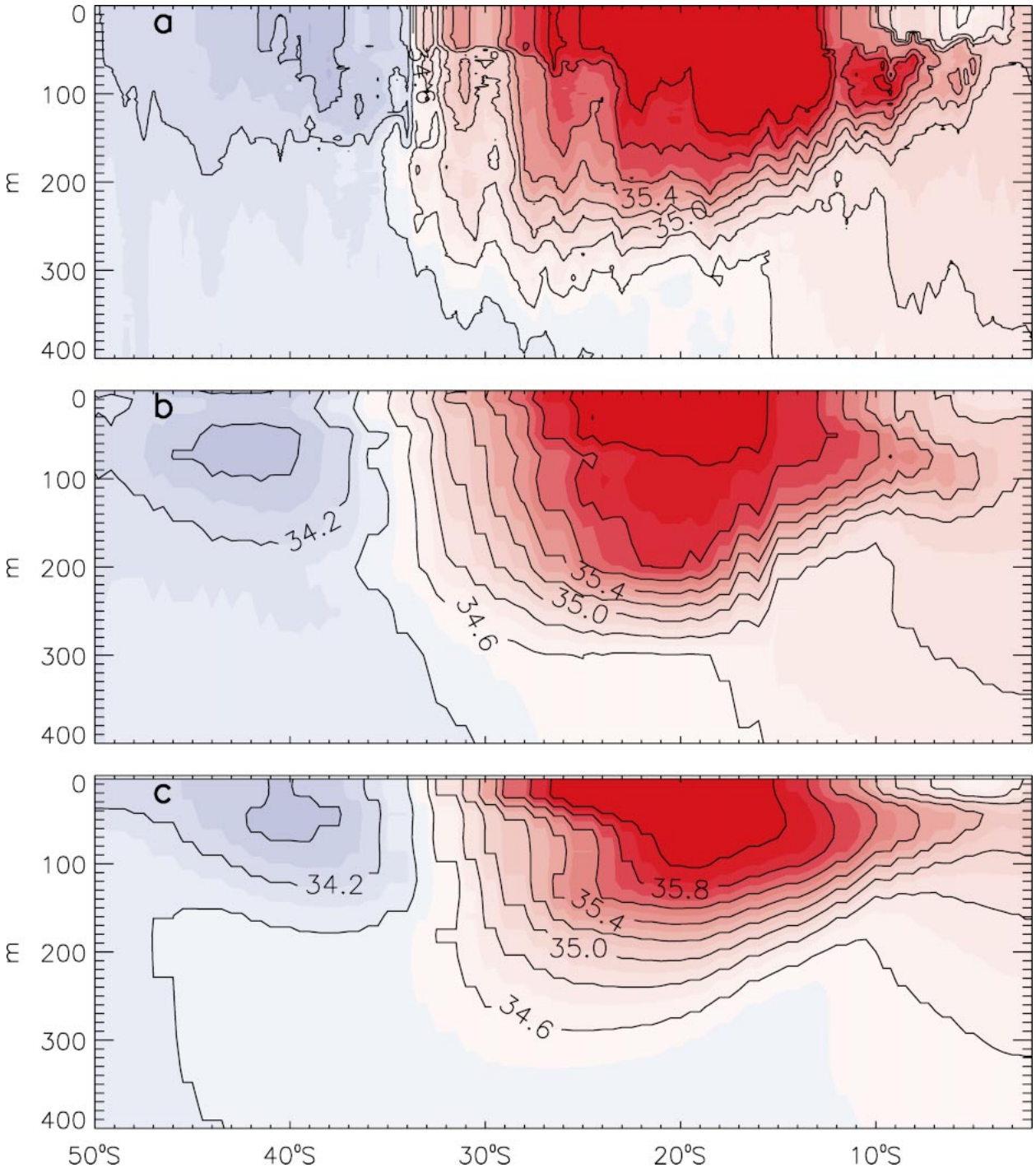

FIG. A1. Upper-ocean salinity (psu) from (a) WOCE line P18 (Feb–Apr 1994), (b) *WOA98* (Mar climatology), and (c) the model (Mar mean 1994).

be compared directly with observations only in March, thanks to two nearby WOCE hydrographic meridional sections. As shown in Fig. 3, P18 from 1994 is to the west along longitude 103°W, whereas P19 from 1993 is to the east at 88°W. The *WOA98* database appears to include the P19 section, but not P18.

These limited data do support the position that the model produces a faithful representation of many aspects of the background temperature, salinity, and density of the SEP region. A comparison of upper-ocean salinity from WOCE P18, *WAO98*, and the model is presented in Fig. A1. Model and *WAO98* profiles have

been interpolated to the track locations, and match the approximate midpoint of observation dates. The *WAO98* climatological March salinity is shown along with the model result from March of 1994. The same range of contours appear in all three sections (34.0–36.0 psu). The similarity of P18 and *WAO98* may not be surprising, given the presence of P19 and little else in the salinity database. But, the agreement with a model that has lost all memory of its initial conditions is not necessarily expected, and is likely as much a testament to the freshwater forcing and precipitation corrections (section 2) as to the model physics. Integrations with different forcing (not shown) indicate that the restoring to surface salinity is far too weak to constrain this salinity field to be in the observed range. There is some agreement in detail between the model and P18, including the high-salinity surface cap extending from about 32° to 10°S, the double halocline between about 35° and 22°S, and the salinity maximum above 100 m north of about 13°S.

The most important feature of the model solution for present purposes is the destabilizing vertical salinity gradient, because it is the key element of the spiciness-generating mixing mechanism. Fortunately, it appears to be well represented in the model (Fig. A1). This gradient must be present for compression into a sharp front at the base of the winter mixed layer, and hence for diapycnal injection onto subducted isopycnals. Although the model $S(0\text{ m}) - S(200\text{ m})$ (Fig. 3) shows broad similarity with *WAO98* in a global sense, locally in the SEP region it is ≈0.4 psu larger. One very likely explanation for this discrepancy is the poor sampling of the *WAO98* database, especially of salinity. In the absence of nearby samples and of observations throughout the year, *WAO98* processing necessarily produces unreliable monthly and annual estimates on its regular grid. The problem in the SEP region is illustrated by the unstable density difference between the surface and 200-m depth in Fig. 4, even though none of the individual profiles in the database are allowed to be unstable. Also, the spatial smoothing of *WAO98* tends to reduce extrema.

Another potential contributor to the difference in the salinity gradient to 200 m is that this depth falls within the halocline in the SEP region, as evident in Figs. 5 and A1, so that small vertical displacements result in large differences in the salinity at 200 m. The situation in March along the WOCE lines is shown in Fig. A2. The greater salinity difference in the model compared to P18 is largely due to its shallower halocline (Fig. A1), while the smaller *WAO98* difference results from its deeper halocline. There is much better agreement across the entire unstable halocline, with the surface to 300 m salinity difference at 20°S about 1.4 psu in all three cases. There are no significant discrepancies in the unstable gradient region of P19 (Fig. A2). In September, the CTD cast shown in Fig. 10 implies a $S(0\text{ m}) - S(200\text{ m})$ of ≈1 psu, while the mean model and *WAO98* differences for this location are 1.0 and 0.86 psu, respectively.

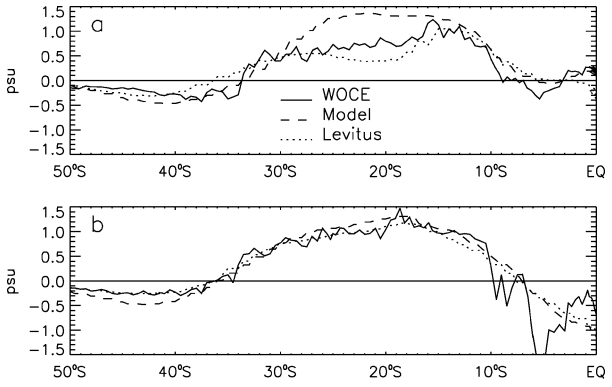

FIG. A2. Upper-ocean salinity gradients S(0 m) − S(200 m) (psu) along (a) WOCE P18 track line and (b) WOCE P19 track line.

APPENDIX B

Vertical Mixing Sensitivity Analysis

This appendix addresses the issue of model fidelity with regard to the vertical mixing that produces the late winter spice anomalies. This issue is of particular importance, because the model results cannot be directly verified by observations. Of most value would be ocean turbulence measurements from the SEP region in the critical mixing month of September, but such data are not available. In the absence of direct microstructure measurements, an attractive alternative would be to compare the model's KPP mixing scheme (section 2) with a large-eddy simulation as winter cooling erodes the stabilizing temperature gradient in the presence of a strongly destabilizing salinity gradient. This comparison is being initiated but is beyond the scope of the present work. However, a one-dimensional (1D) model (Large et al. 1994) of vertical mixing in the SEP region has been used to demonstrate a lack of sensitivity to model vertical resolution, and the small effects of parameterized double diffusion. The results are presented in Figs. B1 and B2.

The 1D mixing is identical to the vertical mixing in the full three-dimensional global model (section 2). For direct comparison with the hindcast event of 1967 (Fig. 5), the 1D model was initialized with the global model solution at 23°S, 258°E from day 100 of 1967. Daily atmospheric fields from the same year and location were used to force the 1D model, which was integrated with a 1-h time step and a depth of 250 m. Changes in overall inventories result primarily from the surface fluxes of momentum, heat and freshwater, and very little from computed fluxes across 250-m depth. The 1D control (Fig. B1c) has exactly the same vertical physics and resolution (15 levels stretched unevenly over the upper 250 m) as the global version. However, it has neither lateral transports nor vertical advection, and so its so-

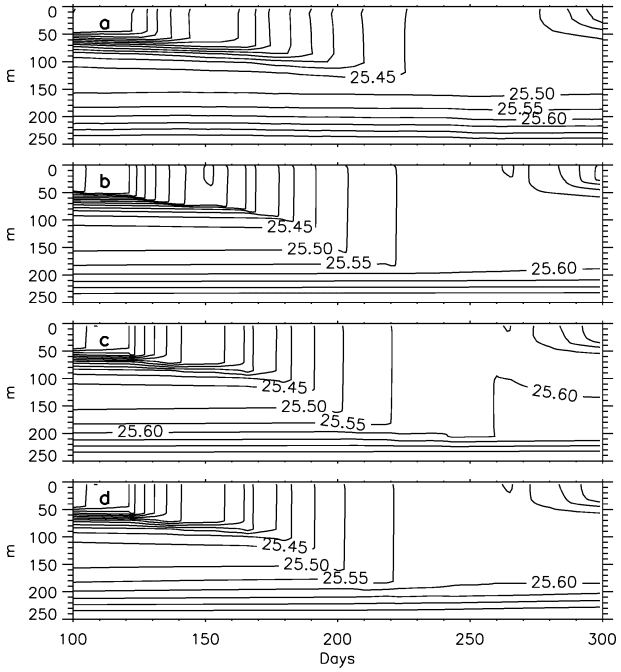

FIG. B1. Comparison of density evolution from day 100 of 1967 at 23°S, 258°E from (a) full 3D model solution, (b) 1D KPP model with 2-m vertical resolution (126 levels in upper 250 m), (c) 1D KPP model with the same vertical grid as full 3D model (15 levels in upper 250 m), and (d) same as (c) but with double diffusion parameterization turned on.

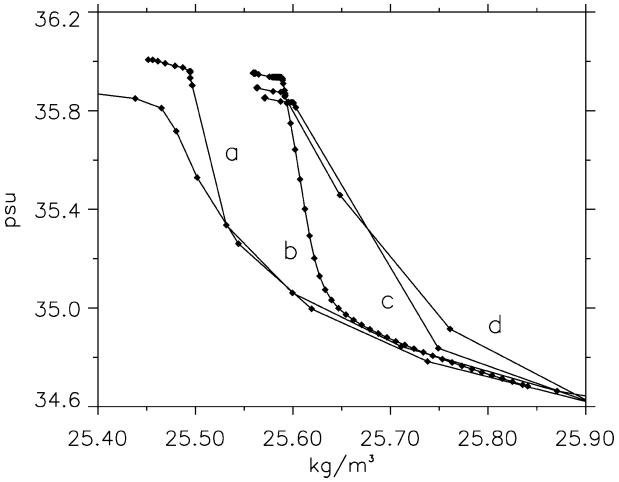

FIG. B2. Water column salinity at 23°S, 258°E as a function of density at day 270 for each case of Fig. B1. The unlabeled profile represents the column at day 100 (common to all four model realizations).

lution continuously diverges from the hindcast (Fig. B1a).

Two sensitivity realizations of the 1967 mixing event were computed: a case (Fig. B1b) with 126 vertical levels in the top 250 m (2-m vertical resolution) and another (Fig. B1d) with parameterized double diffusion below the boundary layer. Only the salt-fingering regime (warm-salty over cold fresh) is relevant here, and the associated diffusivities for salt K_S and heat K_T are a fit to ocean measurements (St. Laurent and Schmitt 1999):

$$K_S(R_\rho) = 1.0 \text{ cm}^2 \text{ s}^{-1}\left[1 - \left(\frac{R_\rho - 1}{2.55 - 1}\right)\right]^3 \quad \text{(B1)}$$

and

$$K_T = 0.7\, K_S. \quad \text{(B2)}$$

Comparison of the global solution (Fig. B1a) and the control (Fig. B1c) indicates that the lateral transports tend to stabilize the water column by reducing the upper density field, which inhibits winter mixing. As a result, $\sigma_0 = 25.5$ in Fig. B1a remains subducted below the mixed layer throughout the winter but outcrops in the other 1D cases. All of the 1D cases show a deeper winter mixed layer and a slight phase shift in the period of maximum mixing in comparison with the full model result. Otherwise, all the solutions display similar behavior, suggesting that vertical processes are dominant and that sensitivities relative to the control are applicable to the global model. In particular, low R_ρ values are generated at the base of the winter mixed layer in each of the three 1D cases, with sharp gradients of T and S coinciding at the lower boundary of well-mixed water (not shown).

Comparison of the control with Figs. B1b and B1d show that there is relatively little sensitivity to vertical resolution and salt fingering, at least on the seasonal timescale. A more detailed examination of how these sensitivities effect the winter generation of spiciness on subducted isopycnals is presented in Fig. B2, which shows the salinity injection given by the difference between the common day 100 curve and the day 270 curves. In all 1D cases, the maximum injection occurs on isopycnals near 25.6, where the salinity increases by about 0.8 psu, even though the depth of the 25.6 isopycnal remains approximately constant at 200 m. The density-lowering lateral processes in the full 3D realization shift the salinity injection to a lower density band altogether. High vertical resolution does keep the gain in salinity confined to a narrow range of isopycnals. The low-resolution vertical grid does not sufficiently resolve the densities at the base of the mixed layer, and the use of a linear interpolation between the isopycnals at vertical grid levels is not a robust measure of the salinity gain at higher densities. The effect of salt fingering appears to broaden the band of the spiciness injection to higher densities, but again there is little effect on the maximum change in isopycnal salinity.

REFERENCES

Arbic, B. K., and W. B. Owens, 2001: Climatic warming of Atlantic intermediate waters. *J. Climate*, **14,** 4091–4108.

Barnett, T. P., D. W. Pierce, M. Latif, D. Dommenget, and R. Saravanan, 1999: Interdecadal interactions between the tropics and midlatitudes in the Pacific basin. *Geophys. Res. Lett.,* **26,** 615–618.

Bindoff, N. L., and J. A. Church, 1992: Warming of the water column in the southwest Pacific Ocean. *Nature,* **357,** 59–62.

——, and T. J. McDougall, 1994: Diagnosing climate change and ocean ventilation using hydrographic data. *J. Phys. Oceanogr.,* **24,** 1137–1152.

——, and ——, 2000: Decadal changes along an Indian Ocean section at 32°S and their interpretation. *J. Phys. Oceanogr.,* **30,** 1207–1222.

Bishop, J. K., and W. B. Rossow, 1991: Spatial and temporal variability of global surface solar irradiance. *J. Geophys. Res.,* **96,** 16 839–16 858.

——, ——, and E. G. Dutton, 1997: Surface solar irradiance from the International Satellite Cloud Climatology Project 1983–1991. *J. Geophys. Res.,* **102,** 6883–6910.

Blanke, B., and S. Raynaud, 1997: Kinematics of the Pacific equatorial undercurrent: An Eulerian and Lagrangrian approach from GCM results. *J. Phys. Oceanogr.,* **27,** 1038–1053.

Bryden, H. L., M. J. Griffiths, A. M. Lavin, R. C. Millard, G. Parrilla, and W. M. Smethie, 1996: Decadal changes in water mass characteristics at 24°N in the subtropical North Atlantic Ocean. *J. Climate,* **9,** 3162–3186.

——, E. L. McDonagh, and B. A. King, 2003: Changes in ocean water mass properties: Oscillations or trends? *Science,* **300,** 2086–2088.

Conkright, M. E., and Coauthors, 2002: *Introduction. World Ocean Database 2001,* Vol. 1, S. Levitus, Ed., NOAA Atlas NESDIS 42, U.S. Government Printing Office, 167 pp.

Danabasoglu, G., J. C. McWilliams, and W. G. Large, 1996: Approach to equilibrium in accelerated global oceanic models. *J. Climate,* **9,** 1092–1110.

Deser, C., M. Alexander, and M. Timlin, 1996: Upper-ocean thermal variations in the North Pacific during 1970–1991. *J. Climate,* **9,** 1840–1855.

Doney, S. C., S. Yeager, G. Danabasoglu, W. G. Large, and J. C. McWilliams, 2003: Modeling global oceanic inter-annual variability (1958–1997): Simulation design and model-data evaluation. NCAR Tech. Note, NCAR/TN-452+STR, 48 pp. [Available from NCAR, P.O. Box 3000, Boulder, CO 80307.]

Fine, R., W. Peterson, and H. Ostlund, 1987: The penetration of tritium into the tropical Pacific. *J. Phys. Oceanogr.,* **17,** 553–564.

Gent, P. R., and J. C. McWilliams, 1990: Isopycnal mixing in ocean circulation models. *J. Phys. Oceanogr.,* **20,** 150–155.

——, F. O. Bryan, G. Danabasoglu, S. C. Doney, W. R. Holland, W. G. Large, and J. C. McWilliams, 1998: The NCAR Climate System Model global ocean component. *J. Climate,* **11,** 1287–1306.

Gu, D., and S. Philander, 1997: Interdecadal climate fluctuations that depend on exchanges between the tropics and extratropics. *Science,* **275,** 805–807.

Harper, S., 2000: Thermocline ventilation and pathways of tropical-subtropical water mass exchange. *Tellus,* **52A,** 330–345.

Hautala, S., and D. Roemmich, 1998: Subtropical mode water in the Northeast Pacific basin. *J. Geophys. Res.,* **103,** 13 055–13 066.

Johnson, G. C., and A. H. Orsi, 1997: Southwest Pacific Ocean water-mass changes between 1968/69 and 1990/91. *J. Climate,* **10,** 306–316.

——, and M. McPhaden, 1999: Interior pycnocline flow from the subtropical to the equatorial Pacific Ocean. *J. Phys. Oceanogr.,* **29,** 3073–3089.

Kalnay, E., and Coauthors, 1996: The NCEP/NCAR 40-Year Reanalysis Project. *Bull. Amer. Meteor. Soc.,* **77,** 437–471.

Kessler, W., 1999: Interannual variability of the subsurface high salinity tongue south of the equator at 165°E. *J. Phys. Oceanogr.,* **29,** 2038–2049.

Kleeman, R., J. P. McCreary Jr., and B. A. Klinger, 1999: A mechanism for generating ENSO decadal variability. *Geophys. Res. Lett.,* **26,** 1743–1746.

Large, W. G., J. C. McWilliams, and S. C. Doney, 1994: Oceanic vertical mixing: A review and a model with a nonlocal boundary layer parameterization. *Rev. Geophys.,* **32,** 363–403.

——, G. Danabasoglu, S. C. Doney, and J. C. McWilliams, 1997: Sensitivity to surface forcing and boundary layer mixing in a global ocean model: Annual-mean climatology. *J. Phys. Oceanogr.,* **27,** 2418–2447.

——, ——, J. C. McWilliams, P. R. Gent, and F. O. Bryan, 2001: Equatorial circulation of a global ocean climate model with anisotropic horizontal viscosity. *J. Phys. Oceanogr.,* **31,** 518–536.

Lazar, A., R. Murtugudde, and A. J. Busalacchi, 2001: A model study of temperature anomaly propagation from the subtropics to tropics within the South Atlantic thermocline. *Geophys. Res. Lett.,* **28,** 1271–1274.

Levitus, S., T. Boyer, M. Conkright, D. Johnson, T. O'Brien, J. Antonov, C. Stephens, and R. Gelfeld, 1998: *Introduction. World Ocean Database 1998,* Vol. 1, NOAA Atlas NESDIS 18, U.S. Government Printing Office, 346 pp.

Liu, Z., S. G. H. Philander, and R. C. Pacanowski, 1994: A GCM study of tropical–subtropical upper-ocean water exchange. *J. Phys. Oceanogr.,* **24,** 2606–2623.

Lu, P., and J. P. McCreary Jr., 1995: Influence of the ITCZ on the flow of thermocline water from the subtropical to the equatorial Pacific Ocean. *J. Phys. Oceanogr.,* **25,** 3076–3088.

Lysne, J., and C. Deser, 2002: Wind-driven thermocline variability in the Pacific: A model-data comparison. *J. Climate,* **15,** 829–845.

——, P. Chang, and B. Giese, 1997: Impact of the extratropical Pacific on equatorial variability. *Geophys. Res. Lett.,* **24,** 2589–2592.

McWilliams, J. C., and G. Danabasoglu, 2002: Eulerian and eddy-induced meridional overturning circulations in the Tropics. *J. Phys. Oceanogr.,* **32,** 2054–2071.

Nonaka, M., and K. Takeuchi, 2001: Tropical subsurface salinity and tritium distributions in the Pacific: Their differences and formation mechanisms. *J. Phys. Oceanogr.,* **31,** 1388–1395.

Pierce, D. W., T. P. Barnett, and M. Latif, 2000: Connections between the Pacific Ocean Tropics and midlatitudes on decadal timescales. *J. Climate,* **13,** 1173–1194.

Provost, C., C. Escoffier, K. Maamaatuaiahutapu, A. Kartavtseff, and V. Garcon, 1999: Subtropical mode waters in the South Atlantic Ocean. *J. Geophys. Res.,* **104,** 21 033–21 049.

Redi, M. H., 1982: Oceanic isopycnal mixing by coordinate rotation. *J. Phys. Oceanogr.,* **12,** 1154–1158.

Rintoul, S. R., and M. H. England, 2002: Ekman transport dominates local air–sea fluxes in driving variability of subantarctic mode water. *J. Phys. Oceanogr.,* **32,** 1308–1321.

Roemmich, D., and B. Cornuelle, 1992: The Subtropical Mode Waters of the South Pacific Ocean. *J. Phys. Oceanogr.,* **22,** 1178–1187.

——, and J. Gilson, 2001: Eddy transport of heat and thermocline waters in the North Pacific: A key to interannual/decadal climate variability? *J. Phys. Oceanogr.,* **31,** 675–688.

Rossow, W. B., and R. A. Schiffer, 1991: ISCCP Cloud Data Products. *Bull. Amer. Meteor. Soc.,* **72,** 2–20.

Rothstein, L. M., R. H. Zhang, A. J. Busalacchi, and D. Chen, 1998: A numerical simulation of the mean water pathways in the subtropical and tropical Pacific Ocean. *J. Phys. Oceanogr.,* **28,** 322–343.

Schmitt, R., 1981: Form of the temperature–salinity relationship in the central water: Evidence for double-diffusive mixing. *J. Phys. Oceanogr.,* **11,** 1015–1026.

Schneider, N., 2000: A decadal spiciness mode in the tropics. *Geophys. Res. Lett.,* **27,** 257–260.

——, A. Miller, M. Alexander, and C. Deser, 1999: Subduction of decadal North Pacific temperature anomalies: Observations and dynamics. *J. Phys. Oceanogr.,* **29,** 1056–1070.

Siedler, G., A. Kuhl, and W. Zenk, 1987: The Madeira Mode Water. *J. Phys. Oceanogr.,* **17,** 1561–1570.

Spencer, R. W., 1993: Global oceanic precipitation from the MSU

during 1979–91 and comparisons to other climatologies. *J. Climate,* **6,** 1301–1326.

St. Laurent, L., and R. W. Schmitt, 1999: The contribution of salt fingers to vertical mixing in the North Atlantic tracer release experiment. *J. Phys. Oceanogr.,* **29,** 1404–1424.

Suga, T., A. Kato, and K. Hanawa, 2000: North Pacific Tropical Water: Its climatology and temporal changes associated with the climate regime shift in the 1970s. *Progress in Oceanography,* Vol. 47, Pergamon, 223–256.

Tsuchiya, M., and L. Talley, 1998: A Pacific hydrographic section at 88°W: Water-property distribution. *J. Geophys. Res.,* **103,** 12 899–12 918.

Xie, P., and P. A. Arkin, 1996: Analyses of global monthly precipitation using gauge observations, satellite estimates, and numerical model predictions. *J. Climate,* **9,** 840–858.

Wong, A. P. S., and G. C. Johnson, 2003: South Pacific Eastern Subtropical Mode Water. *J. Phys. Oceanogr.,* **33,** 1493–1509.

——, N. L. Bindoff, and J. A. Church, 1999: Large-scale freshening of intermediate waters in the Pacific and Indian oceans. *Nature,* **400,** 440–443.

Zhang, R., L. M. Rothstein, and A. J. Busalacchi, 1998: Origin of upper-ocean warming and El Nino change on decadal scales in the tropical Pacific Ocean. *Nature,* **391,** 879–883.